

# Probing orbits of stellar mass objects deep in galactic nuclei with quasi-periodic eruptions – III: Long term evolution

Cong Zhou,<sup>1,2,\*</sup> Yuhe Zeng,<sup>3,4</sup> and Zhen Pan<sup>3,4,†</sup>

<sup>1</sup>CAS Key Laboratory for Research in Galaxies and Cosmology, Department of Astronomy, University of Science and Technology of China, Hefei 230026, P. R. China

<sup>2</sup>School of Astronomy and Space Sciences, University of Science and Technology of China, Hefei 230026, P. R. China

<sup>3</sup>Tsung-Dao Lee Institute, Shanghai Jiao-Tong University, Shanghai, 520 Shengrong Road, 201210, People's Republic of China

<sup>4</sup>School of Physics & Astronomy, Shanghai Jiao-Tong University, Shanghai, 800 Dongchuan Road, 200240, People's Republic of China

(Dated: November 28, 2024)

Quasi-periodic eruptions (QPEs) are intense repeating soft X-ray bursts with recurrence times about a few hours to a few weeks from galactic nuclei. More and more analyses show that QPEs are the result of collisions between a stellar mass object (SMO, a stellar mass black hole or a main sequence star) and an accretion disk around a supermassive black hole (SMBH) in galactic nuclei. QPEs have shown to be invaluable in probing the orbits of SMOs in the vicinity of SMBHs, and further inferring the formation of extreme mass ratio inspirals (EMRIs). In this paper, we extend previous orbital analyses in Refs. [1, 2] by including extra effects, the SMO orbital decay due to collisions with the disk and the disk precession. We find clear Bayes evidence for orbital decay in GSN 069 and for disk precession in eRO-QPE2, the two most stable QPE sources. The detection of these effects provides informative constraints on the SMBH mass, the radiation efficiency of QPEs, the SMO nature, the accretion disk surface density and the accretion disk viscosity. With tighter constraints on the SMO orbital parameters, we further confirm that these two QPE EMRIs are nearly circular orbiters which are consistent with the wet EMRI formation channel prediction, but are incompatible with either the dry loss-cone channel or the Hills mechanism. Combining all the QPE sources available, we find the QPE EMRIs can be divided into two populations according to their orbital eccentricities, where the orbital periods and the SMBH masses in the low-eccentricity population follow a scaling relation  $T_{\text{orb}} \propto M_{\bullet}^n$  with  $n \approx 0.8$ .

## I. INTRODUCTION

Quasi-periodic eruptions (QPEs) are intense repeating soft X-ray bursts with recurrence times about a few hours to a few weeks from galactic nuclei. Since the first detection more than a decade ago [3], QPEs from about ten different nearby galactic nuclei have been reported [4–12]. QPEs are similar in their electromagnetic emissions, with the peak luminosity ( $10^{42} - 10^{43}$  ergs  $s^{-1}$ ), the thermal-like X-ray spectra with temperature  $kT \approx 100 - 250$  eV, the temperature 50–80 eV in the quiescent state, and mild asymmetries between the fast rise and slower decay phases in the flare light curves.

There are several pieces of observational evidence suggesting a strong connection between QPEs and tidal disruption events (TDEs). Both QPEs and TDEs are preferentially found in low-mass poststarburst galaxies which harbor a low-mass ( $\approx 10^5 - 10^7 M_{\odot}$ ) central supermassive black holes (SMBH) [13–15], and an extended emission line region (EELR) [16, 17]. Similar to TDE host galaxies, QPE hosts are of similar morphological properties that are rarely found in broader galaxy population [18]. A stronger QPE-TDE connection is established from the association of QPE sources (GSN 069, XMMSL1 J024916.6-04124, eRO-QPE3, AT2019qiz and a candidate AT 2019vcb) with previous TDEs [11, 12, 15, 19–22]. In particular, QPEs have been directly

detected in X-ray light curves of two TDEs  $O(1)$  years after their ignitions [12, 22].

There is also observational evidence suggesting a likely connection between QPEs/TDEs and a recent accretion phase of the central SMBH. The presence of a narrow line region and the absence of luminous broad emission lines in most QPE host galaxies implies the hosts are recently switched-off active galactic nuclei (AGNs), and a long-lived accretion flow likely plays a role in the QPE phenomenon [14]. The high occurrence of EELRs in both TDE hosts and QPE hosts further implies high (detection) rates of TDEs and QPEs in recently switched-off AGNs [16, 17, 23].

In addition to these common properties of QPE emission spectra and QPE host galaxies, QPE light curves also share some intriguing features that may reveal the QPE origin(s), including the alternating peak luminosities  $I_{\text{strong}}$  and  $I_{\text{weak}}$  and the alternating recurrence times  $T_{\text{long}}$  and  $T_{\text{short}}$ . For example, in the most famous QPE source GSN 069, both  $T_{\text{long}}$  and  $T_{\text{short}}$  show large variations, while  $T_{\text{long}} + T_{\text{short}}$  is approximately a constant [1, 2] (paper I and II hereafter). This observation clearly shows that the period of the underlying dynamical process is actually  $T_{\text{long}} + T_{\text{short}}$  rather than  $T_{\text{long}}$  or  $T_{\text{short}}$ , and two flares with non-uniform intervals are produced in one dynamical period. Besides these common properties shared by most QPEs, a number of peculiar features in several QPE sources have been revealed by long term observations, including the disappearance and reappearance of QPEs and their association with the quiescent state luminosity, the large change in the QPE recurrence times  $T_{\text{long,short}}$ , the complex rising and decay profiles of QPE light curves and the non-uniform de-

\* dysania@mail.ustc.edu.cn

† zhpan@sjtu.edu.cn

cay in the flare recurrence times (see [24, 25] for GSN 069, [7, 26, 27] for eRO-QPE 1, [28, 29] for eRO-QPE 2 and [30] for RX J1301).

These observations provide informative clues on the origin(s) of QPEs. A natural explanation is that QPEs are the result of collisions between a stellar mass object (SMO, a stellar mass black hole or a main sequence star) orbiting around a SMBH in galactic nuclei and an accretion disk, which may be fed by a tidal disruption event or in some cases a recently turn-on AGN disk (see the analysis of Swift J023017 in paper II). Though this EMRI+disk model is not the only interpretation proposed, it is favored by more and more analyses (see e.g., Refs. [1, 2, 10, 11, 27–35] for details). If the EMRI+disk interpretation is correct, QPEs will be a sensitive probe to orbits of SMOs in the vicinity of SMBHs, the SMBH masses, and consequently to formation processes of EMRIs [1, 2] and their formation rates [36, 37].

In previous analyses of the orbits of QPE EMRIs, we considered the simplest scenario in which the SMO moves along a geodesic and the accretion disk lies on the equator [1, 2]. We also noticed that these assumptions might be violated in the long run: e.g., we found the posterior of the EMRI orbital period  $T_{\text{obt}}$  in GSN 069 is multi-peaked, which indicates a slow but measurable evolution in the orbital period; we found a clear increase in the orbital period of eRO-QPE1 between Aug. 2020 and Aug. 2021, and we supposed the origin of the apparent orbital period increase is due to nodal precession and alignment of the accretion disk; we also found a clear decrease in the orbital period of eRO-QPE2 between Aug. 2020 and Jun. 2022 and we attributed this apparent orbital period decrease as the SMO orbital energy dissipation as crossing the disk. Recent observations show that apparent orbital period decrease of eRO-QPE2 is non-uniform, thus the modulation of the disk precession seems to play a role [28].

In this work, we extend the previous analyses by including extra effects, the SMO orbital decay due to collisions with the disk, the disk precession and possible alignment of an initially misaligned disk. We find clear Bayes evidence for orbital decay in GSN 069 and evidence for orbital decay or disk alignment in eRO-QPE2, the two most stable QPE sources. Taking these extra effects into account, we can fit multiple observations spanning a long time with the QPE timing model. As a result, we obtain tighter constraints on the SMO orbital parameters than in previous analyses, including the orbital size, the orbital eccentricity and the central SMBH mass. Consistent with previous analyses, we find the two QPE EMRIs are of nearly circular orbits with eccentricity  $e = O(10^{-2})$  and semi-major axis  $A = O(10^2)M_{\bullet}$ , where  $M_{\bullet}$  the gravitational radius of the central SMBH. These orbital parameters are consistent with the wet EMRI formation channel prediction [38–46], but are incompatible with either the dry channel [47–52] or the Hills channel [53, 54]. Collecting 8 QPE sources in total with reasonable measurements of the orbital period  $T_{\text{obt}}$  and the SMBH mass  $M_{\bullet}$ , we find a likely correlation relation  $T_{\text{obt}} \propto M_{\bullet}^{0.8}$  among 6 QPE sources wherein the EMRIs are of low eccentricities.

This paper is organized as follows. In Section II, we introduce the EMRI+disk model. In Section III, we show the

detailed analyses of the two QPE sources. This paper is concluded with Section IV. Throughout this paper, we use the geometrical units with convention  $G = c = 1$ .

## II. EMRI+DISK MODEL

In an EMRI+disk system, one can in principle predict the SMO-disk collision time and the resulting QPE light curve. But the prediction of the light curve is subject to large uncertainties in the disk model, the nature of the SMO and the radiation mechanism. Following papers I and II, we choose to constrain the EMRI kinematics and the QPE emission separately for mitigating the impact of these uncertainties: we first fit each QPE with a simple light curve model and obtain the starting time of each flare  $t_0 \pm \sigma(t_0)$  (see paper II for details of light curve fitting), which is identified as the observed disk crossing time and used for constraining the EMRI orbital parameters assuming a flare timing model.

The flare timing model consists of two major components: the SMO motion and the disk motion. In papers I and II, we have assumed that the SMO moves along a geodesic ignoring the small orbital energy dissipation due to collisions with the disk. As noticed in paper II, the geodesic assumption may be violated in some QPE sources in the long run, where long-term observations are available and the small orbital period decay  $\dot{T}_{\text{obt}}$  may be detectable. In this work, we consider both EMRI geodesics and forced EMRI trajectories where the orbital decay caused by the SMO-disk collisions is taken into account. In papers I and II, we have assumed that the disk lies on the equator, therefore no nontrivial disk motion. Again in paper II, we found an apparent orbital period increase in eRO-QPE 1, which is likely the result of disk precession and alignment. In paper II, we also analyzed another famous QPE source, eRO-QPE 2, and we attributed the apparent orbital period decay from XMM 1 (2020-08-06) to XMM 2 (2022-02-06) and 3 (2022-06-21) the SMO-disk collisions. However, the most recent observation XMM 4 (2023-12-08) shows that the the apparent orbital period decay is nonuniform, and the disk precession likely plays a role here, either modulating the apparent QPE intervals or modulating the SMO orbital decay rate [28]. In this work, we take the precession and alignment of an initially misaligned disk into consideration.

With data  $d = \{t_0^{(k)} \pm \sigma^{(k)}(t_0)\}$  ( $k$  is the flare index) and a flare timing model, we can constrain model parameters  $\Theta$ . According to the Bayes theorem, the posterior of parameters is

$$\mathcal{P}(\Theta, \mathcal{H}|d) = \frac{\mathcal{L}(d|\Theta, \mathcal{H})\pi(\Theta, \mathcal{H})}{\mathcal{Z}(d)}, \quad (1)$$

where  $\mathcal{L}(d|\Theta, \mathcal{H})$  is the likelihood of detecting data  $d$  under hypothesis  $\mathcal{H}$  with model parameters  $\Theta$ ,  $\pi(\Theta, \mathcal{H})$  is the parameter prior assumed, and the normalization factor  $\mathcal{Z}(d)$  is the evidence of hypothesis  $\mathcal{H}$  with data  $d$ . To quantify the support for one hypothesis  $\mathcal{H}_1$  over another  $\mathcal{H}_0$  by data  $d$ , we can define the Bayes factor

$$\mathcal{B}_0^1 = \frac{\mathcal{Z}_1(d)}{\mathcal{Z}_0(d)}. \quad (2)$$

The higher value of  $\mathcal{B}_0^1$  stands for stronger support for hypothesis  $\mathcal{H}_1$  over  $\mathcal{H}_0$ . According to Jeffreys's scale,  $\log \mathcal{B}_0^1 \in (1.2, 2.3), (2.3, 3.5), (3.5, 4.6), (4.6, \infty)$  are the criteria of substantial, strong, very strong, and decisive strength of evidence, respectively.

In the following subsections, we will explain two main components of the flare timing model and define the likelihoods.

### A. EMRI trajectories

If the SMO orbital energy loss is negligible, the SMO simply moves along a geodesic. Otherwise, the SMO moves along a forced trajectory where the extra force arising from collisions with the accretion disk should be taken into account. In this work, we consider both cases and test them against QPE observations.

#### 1. EMRI geodesics

The orbit of a test particle in the Kerr spacetime

$$ds^2 = g_{\mu\nu} dx^\mu dx^\nu, \quad (3)$$

can be obtained by solving the geodesic equation of motion (EoM),

$$\frac{d^2 x^\mu}{d\tau^2} + \Gamma_{\alpha\beta}^\mu \frac{dx^\alpha}{d\tau} \frac{dx^\beta}{d\tau} = 0, \quad (4)$$

where  $\tau$  is the proper time and  $\Gamma_{\alpha\beta}^\mu$  is the Christoffel connection (we will use the Boyer-Lindquist coordinates for the Kerr metric in this work). Equivalently, one can recast the geodesics EoM above as a set of Hamiltonian EoMs as did in papers I and II.

The analytic solution to Kerr geodesics is also available [55, 56] and is more efficient for the purpose of QPE orbital analysis. In terms of Mino time ( $d\lambda = 1/\Sigma d\tau$ ) [57], the equations of motion in the radial and polar direction are decoupled

$$\begin{aligned} \left(\frac{dr}{d\lambda}\right)^2 &= V_r(r), \\ \left(\frac{dz}{d\lambda}\right)^2 &= V_z(z), \\ \frac{dt}{d\lambda} &= \frac{r^2 + a^2}{\Delta} (E(r^2 + a^2) - aL) - a^2 E(1 - z^2) + aL, \\ \frac{d\phi}{d\lambda} &= \frac{a}{\Delta} (E(r^2 + a^2) - aL) + \frac{L}{1 - z^2} - aE, \end{aligned} \quad (5)$$

where  $z = \cos \theta$  and  $\Sigma = r^2 + a^2 z^2$ ,  $\Delta = r(r - 2) + a^2$ . The two potentials  $V_r(r)$  and  $V_z(z)$  are [56]

$$\begin{aligned} V_r(r) &= [(r^2 + a^2)E - aL]^2 - \Delta[r^2 + (L - aE)^2 + C], \\ V_z(z) &= C(1 - z^2) - [(1 - z^2)(1 - E^2)a^2 + L^2]z^2. \end{aligned} \quad (6)$$

where  $E, L, C$  are the integrals of motion: energy, angular momentum and Carter constant [58]. In Refs. [55, 56], the solutions are written as analytic functions of four phases  $\{q_r, q_z, q_t, q_\phi\}$  which evolve linearly with the Mino time, i.e.,

$$\begin{aligned} r(\lambda) &= r(q_r(\lambda); E, L, C), & q_r(\lambda) &= \Upsilon_r \lambda + q_{r,\text{ini}}, \\ z(\lambda) &= z(q_z(\lambda); E, L, C), & q_z(\lambda) &= \Upsilon_z \lambda + q_{z,\text{ini}}, \\ t(\lambda) &= t(q_{t,r,z}(\lambda); E, L, C), & q_t(\lambda) &= \Upsilon_t \lambda + q_{t,\text{ini}}, \\ \phi(\lambda) &= \phi(q_{\phi,r,z}(\lambda); E, L, C), & q_\phi(\lambda) &= \Upsilon_\phi \lambda + q_{\phi,\text{ini}}, \end{aligned} \quad (7)$$

(see Ref. [56] for the explicit expressions of the Mino time frequencies  $\Upsilon_\mu(E, L, C)$  and  $x^\mu(q)$ <sup>1</sup>), where the four frequencies  $\{\Upsilon_r, \Upsilon_z, \Upsilon_t, \Upsilon_\phi\}$  are functions of integrals of motion and therefore are constant themselves, and  $\{q_{r,\text{ini}}, q_{z,\text{ini}}, q_{t,\text{ini}}, q_{\phi,\text{ini}}\}$  are the initial phases. As in paper II, we use the orbital parameters semilatus rectum  $p$ , eccentricity  $e$  and minimum polar angle  $\theta_{\text{min}}$  to label the bound Kerr geodesics. The conversion relations between the integrals of motion ( $E, L, C$ ) and the orbital parameters ( $p, e, \theta_{\text{min}}$ ) have been derived in Ref. [59].

Considering a bound orbit with parameters ( $p, e, \theta_{\text{min}}$ ), we first obtain the integrals of motion ( $E, L, C$ ) using the conversion relations [59], then set the three initial phases  $\{q_{r,\text{ini}}, q_{z,\text{ini}}, q_{\phi,\text{ini}}\}$ , while the initial phase in the time direction  $q_{t,\text{ini}}$  is obtained from  $t(q_{t,\text{ini}}, q_{r,\text{ini}}, q_{z,\text{ini}}) = t_{\text{ini}}$ , where  $t_{\text{ini}}$  is some starting time point and we set  $t_{\text{ini}}$  as (a moment shortly before) the starting time of the first observed flare  $t_0^{(1)}$  in our QPE analyses.

#### 2. Forced EMRI trajectories

Taking the orbital energy dissipation into account as the SMO crosses the accretion disk into account, the SMO does not move along a geodesic any more, i.e., the orbital parameters  $\{p, e, \cos \theta_{\text{min}}\}$  are now time dependent. Similar to the geodesic case, the forced EMRI trajectories can also be computed making use of the analytic formula in the following way,

$$\begin{aligned} r(\lambda) &= r(q_r(\lambda); E, L, C), & \frac{dq_r}{d\lambda} &= \Upsilon_r(E, L, C), \\ z(\lambda) &= z(q_z(\lambda); E, L, C), & \frac{dq_z}{d\lambda} &= \Upsilon_z(E, L, C), \\ t(\lambda) &= t(q_{t,r,z}(\lambda); E, L, C), & \frac{dq_t}{d\lambda} &= \Upsilon_t(E, L, C), \\ \phi(\lambda) &= \phi(q_{\phi,r,z}(\lambda); E, L, C), & \frac{dq_\phi}{d\lambda} &= \Upsilon_\phi(E, L, C), \end{aligned} \quad (8)$$

except that  $\{E, L, C\}$  and the frequencies  $\{\Upsilon_r, \Upsilon_z, \Upsilon_\phi\}$  are now time dependent.

For the SMO-disk collision, the relative changes in orbital parameters are similar in magnitudes with  $\delta e/e \sim \delta T_{\text{obt}}/T_{\text{obt}} \sim \delta \theta_{\text{min}}/\theta_{\text{min}}$  [e.g., 31, 45]. As we will see later, the small fractional change in the orbital period  $\delta T_{\text{obt}}$  is detectable, while  $\delta e$

<sup>1</sup> There is a sign typo in equation (33) of Ref. [56].

and  $\delta\theta_{\min}$  are undetectable for the QPE sources available, because  $T_{\text{obt}}$  is the best constrained orbital parameter. Therefore, we can safely take  $\dot{e} = \dot{\theta}_{\min} = 0$  in solving the EoMs above. As for the orbital period decay rate  $\dot{T}_{\text{obt}}(t)$ , we consider

$$\dot{T}_{\text{obt}}(t) = \dot{T}_{\text{obt,max}} \sin \iota_{\text{sd}}(t), \quad (9)$$

where  $\iota_{\text{sd}}$  the angle between the SMO orbital plane and the disk plane (see Eq. [22]). The former is a leading-order approximation for any slowly varying orbital decay rate. For a precessing misaligned disk,  $\iota_{\text{sd}}$  is expected to be modulated by both the disk precession and the SMO orbital precession, therefore the decay rate  $\dot{T}_{\text{obt}}$  is non-uniform. For a disk on the equator,  $\iota_{\text{sd}}$  is a constant, then the orbital period decay rate is also a constant.

## B. Disk precession and alignment

As a minimal assumption of the disk precession, we model it as a rigid body like precession with a constant precession rate. The normal vector of the disk plane is  $\vec{n}_{\text{disk}} = (\sin\beta \cos\alpha, \sin\beta \sin\alpha, \cos\beta)$ , where  $\alpha \in (0, 2\pi)$  is the azimuth angle and  $\beta \in (0, \pi/2)$  is the angle between the disk plane and the equatorial plane. The azimuth angle then evolves as

$$\alpha(t) = \alpha_{\text{ini}} + \frac{2\pi}{\tau_p}(t - t_{\text{ini}}), \quad (10)$$

where  $\tau_p$  is the disk precession period, and  $\alpha_{\text{ini}}, \beta_{\text{ini}}$  are the initial values of the azimuth and the polar angles specifying the disk orientation at  $t_{\text{ini}}$ .

There is no obvious function form of parameterizing the disk alignment process, i.e.,  $\beta(t)$ . One can in principle constrain  $\beta(t)$  in a non-parametric approach with dense observations of the QPEs, which however are not available for the QPE sources considered in this work. Limited by the amount of information available, we consider two extremal alignment processes: 1) slow alignment where  $\beta(t) = \beta_{\text{ini}}$ ; 2) fast alignment where  $\beta = \beta_{\text{ini}}$  during the 1st observation and  $\beta = 0$  during subsequent observations.

Observable collisions happen when the SMO crosses the surface of the disk facing to the observer, i.e.  $r_{\text{crs}}(\vec{n}_{\text{crs}} \cdot \vec{n}_{\text{disk}}) = H \text{sign}(\vec{n}_{\text{obs}} \cdot \vec{n}_{\text{disk}})$ . Without loss of generality, we fix the observer in the  $x-z$  plane, i.e., the unit direction vector pointing to the observer is  $\vec{n}_{\text{obs}} = (\sin\theta_{\text{obs}}, 0, \cos\theta_{\text{obs}})$ . We can fix the observer in the upper semisphere when considering a disk lying on the equator, i.e.,  $\theta_{\text{obs}} \in (0, \pi/2)$ . The disk height to the mid-plane is set as  $H = 1.5M_{\bullet}$  as in paper II.

## C. Flare timing model

To summarize, we will consider the following hypotheses that are slight different in the SMO motion,

- Free EMRI hypothesis ( $\mathcal{H}_{e0}$ ): The SMO moves along a geodesic around the SMBH, which can be specified by 8 parameters: the intrinsic orbital parameters

( $p, e, \theta_{\min}$ ), the initial phases ( $q_{r,\text{ini}}, q_{z,\text{ini}}, q_{\phi,\text{ini}}$ ), the mass of the SMBH  $M_{\bullet}$  or equivalently the orbital period  $T_{\text{obt}} := 2\pi(A/M_{\bullet})^{3/2}M_{\bullet}$  (with semi-major axis  $A = p/(1 - e^2)$ ), the dimensionless spin of the SMBH  $a$ .

- Forced EMRI hypothesis ( $\mathcal{H}_{e1}$ ): a forced EMRI orbit due to SMO-disk collisions with the orbital period decay rate quantified by an extra parameter  $\dot{T}_{\text{obt}}$  or  $\dot{T}_{\text{obt,max}}$  [Eq. (9)].

and in the disk motion,

- Equatorial disk hypothesis ( $\mathcal{H}_{d0}$ ): a disk simply lies on the equator.
- Misaligned disk hypothesis ( $\mathcal{H}_{\text{df/ds}}$ ): we consider a misaligned disk with an initial orientation in the  $(\alpha_{\text{ini}}, \beta_{\text{ini}})$  direction. The disk precesses with a period  $\tau_p$  and completes the alignment in a fast/slow way ( $\mathcal{H}_{\text{df/ds}}$ ) as explained in the previous subsection.

A full flare timing model consists of an EMRI motion hypothesis and a disk motion hypothesis, e.g., we will consider a vanilla hypothesis ( $\mathcal{H}_0 = \mathcal{H}_{e0} + \mathcal{H}_{d0}$ ) as a reference for every QPE source analyzed in this work.

For a given SMO trajectory and the disk motion, one can calculate the disk crossing times  $t_{\text{crs}}$ , which we identify as the flare starting times. The propagation times of different flares at different collision locations  $r_{\text{crs}}\vec{n}_{\text{crs}}$  to the observer will also be different. Taking the light propagation delays into account, we can write  $t_{\text{obs}} = t_{\text{crs}} + \delta t_{\text{geom}} + \delta t_{\text{shap}}$ , where

$$\begin{aligned} \delta t_{\text{geom}} &= -r_{\text{crs}}\vec{n}_{\text{obs}} \cdot \vec{n}_{\text{crs}}, \\ \delta t_{\text{shap}} &= -2M_{\bullet} \log[r_{\text{crs}}(1 + \vec{n}_{\text{obs}} \cdot \vec{n}_{\text{crs}})], \end{aligned} \quad (11)$$

are corrections caused by different path lengths and different Shapiro delays [60], respectively.

## D. Flare timing likelihood

Following paper II, we introduce a parameter  $\sigma_{\text{sys}}$  quantifying the effect of any physical processes that are relevant but not included in our flare timing model, assuming the unmodeled advances or delays in the flare timing follows a Gaussian distribution with variance  $\sigma_{\text{sys}}^2$ . Similar inference method has been used in the context of hierarchical test of General Relativity with gravitational waves [61]. As a result, the likelihood of seeing data  $d = \{t_0^{(k)}\}$  under hypothesis  $\mathcal{H}$  with model parameters is

$$\mathcal{L}_{\text{timing}}(d|\Theta, \mathcal{H}) = \prod_k \frac{1}{\sqrt{2\pi(\tilde{\sigma}(t_0^{(k)}))^2}} \exp\left\{-\frac{(t_{\text{obs}}^{(k)} - t_0^{(k)})^2}{2(\tilde{\sigma}(t_0^{(k)}))^2}\right\}, \quad (12)$$

where  $(\tilde{\sigma}(t_0^{(k)}))^2 = (\sigma(t_0^{(k)}))^2 + \sigma_{\text{sys}}^2$  is the uncertainty contributed by both modeled and unmodeled uncertainties. We also incorporate the central SMBH mass measurement from



the stellar velocity dispersion using the  $M_\bullet - \sigma_\star$  relation [62, 63] as a contribution to the total likelihood as

$$\mathcal{L}_{M_\bullet}(d|\Theta, \mathcal{H}) = \frac{1}{\sqrt{2\pi\sigma_{\log_{10} M_\bullet}^2}} \exp\left\{-\frac{(\log_{10} M_\bullet - \mu_{\log_{10} M_\bullet})^2}{2\sigma_{\log_{10} M_\bullet}^2}\right\}, \quad (13)$$

where  $\mu_{\log_{10} M_\bullet}$  and  $\sigma_{\log_{10} M_\bullet}$  are the central value and the uncertainty of inferred SMBH mass, respectively (see [14] for a brief summary of the mass measurements of SMBHs in the QPE host galaxies). The total likelihood is therefore  $\mathcal{L}_{\text{timing}} \times \mathcal{L}_{M_\bullet}$ . In this work, unlike in Paper II, we use the *nessai* [64] algorithm within *Bilby* [65] for model parameter inference on GSN 069. For eRO-QPE2, we employ the *pymultinest* [66] algorithm, also within *Bilby*, leveraging its MPI support.

### III. ANALYSES OF QPE SOURCES

#### A. GSN 069

In addition to the 3 XMM-Newton observations used in paper I and II, to better constrain the orbital evolution, we also take the Chandra observation at 2019-02-14 into account in this work. Following paper I and Ref. [24], we process the Chandra data with CIAO software. As has been illustrated in paper I, the light curve profile of Chandra is obviously incomplete, making it hard to locate the flare starting time  $t_0$ . However, given the accurate determination of flare peak time  $t_p$  in Chandra and also XMM-Newton light curve data, we can statistically obtain  $t_p - t_0$  from the XMM-Newton data and subsequently derive  $t_0$  in Chandra data.

Combining 3 XMM-Newton observations and 1 Chandra observation in 2018 and 2019, we first constrain the orbital parameters in GSN 069 under the vanilla hypothesis  $\mathcal{H}_0$  and we find

$$\begin{aligned} p &= 289_{-189}^{+138} M_\bullet, \\ e &= 0.04_{-0.04}^{+0.05}, \\ T_{\text{obt}} &= 63.70_{-0.07}^{+0.02} \text{ ks}, \end{aligned} \quad (14)$$

at 2- $\sigma$  confidence level. The posterior corner plot of all model parameters are shown in Fig. 5. Slightly different from Paper II, we have included the Chandra observation in the orbital analysis here. Though the data quality is not as good as XMM-Newton observations, the three data points added still tighten the parameter constraints.

A natural extension to the vanilla hypothesis is the orbital decay due to the energy loss as the SMO crosses the disk. Under the hypothesis of a forced EMRI+an equatorial disk ( $\mathcal{H}_1 = \mathcal{H}_{e1} + \mathcal{H}_{d0}$ ), we constrain the orbital decay rate  $\dot{T}_{\text{obt}}$  in addition to the orbital parameters as

$$\begin{aligned} p &= 300_{-52}^{+53} M_\bullet, \\ e &= 0.04_{-0.02}^{+0.02}, \\ T_{\text{obt}} &= 64.73_{-0.03}^{+0.02} \text{ ks}, \\ \dot{T}_{\text{obt}} &= -6.5_{-0.2}^{+0.2} \times 10^{-5}, \end{aligned} \quad (15)$$

at 2- $\sigma$  confidence level. The posterior corner plot of all model parameters are shown in Fig. 6. As a result, the orbital period  $T_{\text{obt}}$  is better constrained than in  $\mathcal{H}_0$ . We also find the Bayes factor between the two hypotheses

$$\log \mathcal{B}_0^1 = 5.8 \pm 0.2, \quad (16)$$

2- $\sigma$  confidence level, which is decisive evidence for the non-zero orbital decay.

For comparison, the two best-fit orbits under the two hypotheses are shown in Fig. 1, with orbital parameters  $p = 172 M_\bullet, e = 0.06, T_{\text{obt}} = 63.70$  ks ( $\mathcal{H}_0$ ) and  $p = 279 M_\bullet, e = 0.06, T_{\text{obt}} = 64.74$  ks,  $\dot{T}_{\text{obt}} = -6.5 \times 10^{-5}$  ( $\mathcal{H}_1$ ). Disk precession has also been considered, and analysis of GSN 069 QPEs shows no signature of disk precession.

With the data favored hypothesis  $\mathcal{H}_1$ , the orbital analysis above has a number of immediate applications.

1. *SMBH mass.* One can constrain the SMBH mass from the SMO orbital period  $T_{\text{obt}}$  and the Schwarzschild precession period  $T_{\text{prec}}$ , both of which can be inferred from the QPE timing. The orbital period

$$T_{\text{obt}} = 2\pi(A/M_\bullet)^{3/2} M_\bullet, \quad (17)$$

is the best constrained orbital parameter, which can be easily identified as  $T_{\text{long}} + T_{\text{short}}$ . The apsidal precession period  $T_{\text{prec}}$  is much longer with a ratio

$$\frac{T_{\text{prec}}}{T_{\text{obt}}} = \frac{p}{3M_\bullet} \approx \frac{A}{3M_\bullet}, \quad (18)$$

where the approximation is accurate for low-eccentricity orbits. The apsidal precession period can be inferred from the modulation of  $T_{\text{long}}$  and  $T_{\text{short}}$  (see Fig. 1 in paper I). We find that observations XMM 3-5 span  $\approx 200$  orbital periods, which are sufficiently long to resolve the apsidal precession period,  $T_{\text{prec}} \approx 100T_{\text{obt}}$ . Consequently, both the orbital size  $p$  and the SMBH mass  $M_\bullet$  can be constrained. As a result, we find

$$\log_{10}(M_\bullet/M_\odot) = 5.6_{-0.1}^{+0.1}, \quad (19)$$

at 2- $\sigma$  confidence level, which is consistent with and of much lower uncertainty than the constraint  $\log_{10}(M_\bullet/M_\odot) = 6.0 \pm 1.0$  (at 2- $\sigma$  confidence level) inferred from the  $M_\bullet - \sigma_\star$  relation [14]. This QPE timing method is promisingly of wide applications in measuring SMBH masses considering the simple physics [Eqs. (17,18)] it involves and the high rate of QPEs. We will elaborate this point in a forthcoming paper.

2. *QPE radiation efficiency.* In terms of the amount of orbital energy loss  $E_{\text{col}}$  per collision, we find

$$E_{\text{col}} = \frac{E_{\text{obt}}}{3} \dot{T}_{\text{obt}} = 6.5_{-1.3}^{+1.3} \times 10^{46} \left(\frac{m}{M_\odot}\right) \text{ ergs}, \quad (20)$$

where  $E_{\text{obt}} = -GM_\bullet m/2A$  is the SMO orbital energy. In combination with the estimation of total energy radiated during one QPE flare [24],  $E_{\text{QPE}} \approx 6.7 \times 10^{45}$  ergs, we obtain a high QPE radiation efficiency

$$\eta_{\text{QPE}} = \frac{E_{\text{QPE}}}{E_{\text{col}}} \approx 10_{-2}^{+2} \% \times \left(\frac{m}{M_\odot}\right)^{-1}, \quad (21)$$

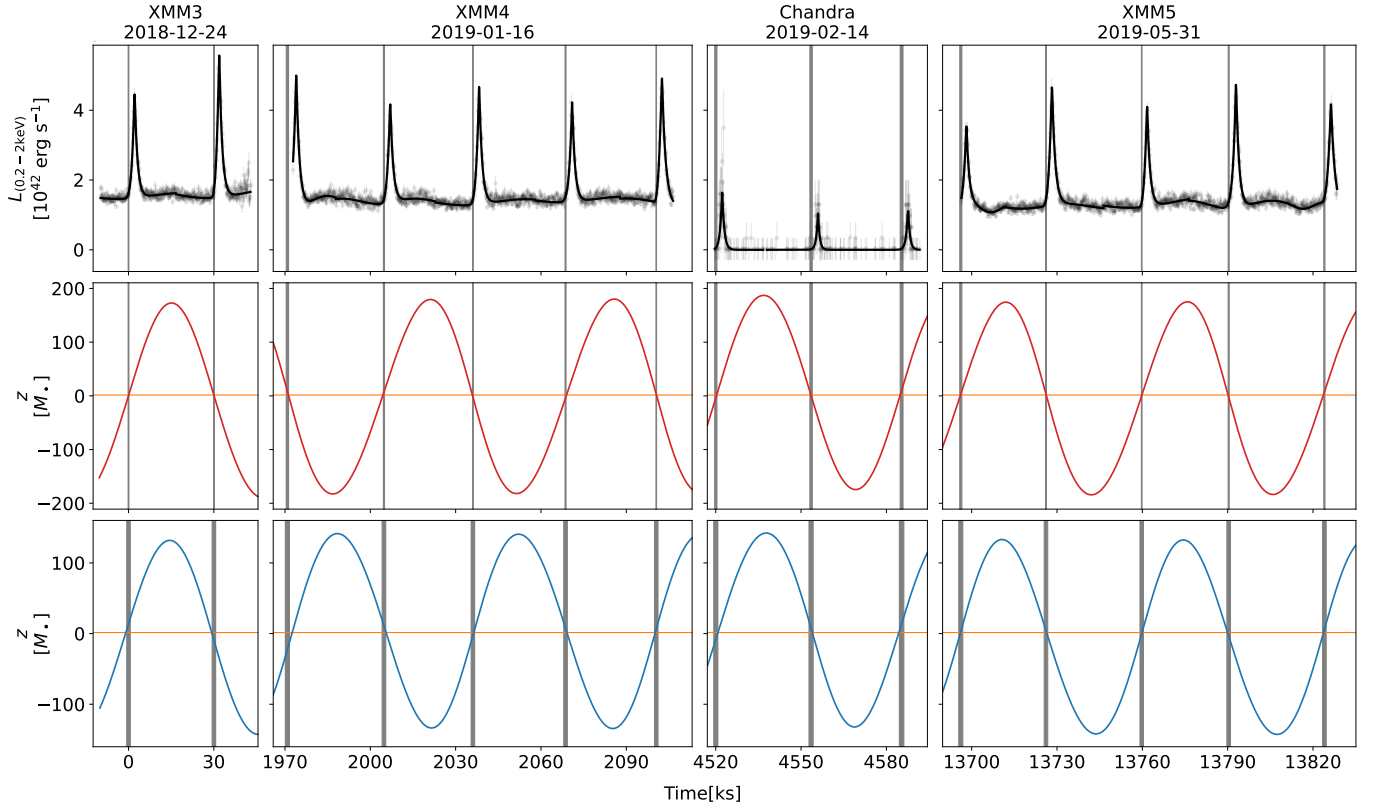


FIG. 1. Top panel: light curve data of GSN 069 along with the best-fit EMRI trajectories, where the vertical bands are the inferred starting times  $t_0^{(k)} \pm \sigma(t_0^{(k)})$  of the QPEs. Mid/Bottom panel: distance to the disk midplane  $z_{\text{disk}}(t)$  of the best-fit orbits, where the orange horizontal lines denote the disk surface  $z = H$  and the vertical bands are the inferred starting times  $t_0^{(k)} \pm \tilde{\sigma}(t_0^{(k)})$ , with  $\tilde{\sigma}(t_0^{(k)}) = \sqrt{(\sigma(t_0^{(k)}))^2 + \sigma_{\text{sys}}^2}$ . Red: forced EMRI hypothesis ( $\mathcal{H}_1$ ). Blue: vanilla hypothesis ( $\mathcal{H}_0$ ).

at 2- $\sigma$  confidence level, which yields a tight constraint on possible QPE radiation mechanisms. Note that both the orbital energy loss  $E_{\text{col}}$  and the total radiation energy  $E_{\text{QPE}}$  are observables read from the QPE light curves.

3. *Disk surface density.* Equating the measured orbital energy loss  $E_{\text{col}}$  per collision to the theoretical expectation if the SMO is a normal star (paper I)

$$\begin{aligned} \delta E_{\star} &= 2 \times \frac{1}{2} \delta m_{\text{gas}} v_{\text{rel}}^2 \\ &\approx 10^{46} \text{ ergs} \times \Sigma_5 R_{\star, \odot}^2 r_{300}^{-1} \sin \iota_{\text{sd}}, \end{aligned} \quad (22)$$

we find the disk surface density

$$\Sigma_5 \approx 6.5_{-1.3}^{+1.3} m_{\star, \odot} R_{\star, \odot}^{-2} r_{300} (\sin \iota_{\text{sd}})^{-1}, \quad (23)$$

where  $\delta m_{\text{gas}}$  is the amount of gas shocked by the star,  $v_{\text{rel}}$  is the relative velocity between the star and the local gas during collision,  $\Sigma_5 = \Sigma / (10^5 \text{ g cm}^{-2})$ ,  $m_{\star, \odot} = m_{\star} / M_{\odot}$ ,  $R_{\star, \odot} = R_{\star} / R_{\odot}$  and  $r_{300} = r / 300 M_{\odot}$ .

4. *Accretion disk viscosity.* We consider the standard thin disk model [67], where the disk structure in the radiation dom-

inated regime can be analytically expressed as [68]

$$\begin{aligned} \Sigma_5 &= 1.7 \alpha_{0.01}^{-1} \dot{M}_{\bullet, 0.1}^{-1} r_{100}^{3/2}, \\ &= 3.5 \left( \frac{\alpha}{0.1} \right)^{-1} \left( \frac{L_{\text{bgd}}}{10^{42} \text{ ergs s}^{-1}} \right)^{-1} \left( \frac{T_{\text{obt}}}{64 \text{ ks}} \right), \end{aligned} \quad (24)$$

for  $\alpha$ -disks, where  $\dot{M}_{\bullet, 0.1} = \dot{M}_{\bullet} / (0.1 \dot{M}_{\bullet, \text{Edd}})$  with  $\dot{M}_{\bullet, \text{Edd}}$  the Eddington accretion rate, and we have used the background luminosity  $L_{\text{bgd}} = 10^{37} \text{ ergs s}^{-1} \times (M_{\bullet} / M_{\odot}) \dot{M}_{\bullet, 0.1}$ . Combining Eqs.(23) and (24), we obtain  $\alpha \approx 0.05$  for the  $\alpha$ -disk model.

In the same way, we consider  $\beta$ -disks with surface density profile [68]

$$\begin{aligned} \Sigma_5 &= 3.2 \alpha_{0.1}^{-4/5} \dot{M}_{\bullet, 0.1}^{3/5} M_{\bullet, 0.5}^{1/5} r_{100}^{-3/5}, \\ &= 0.95 \left( \frac{\alpha}{0.1} \right)^{-4/5} \left( \frac{L_{\text{bgd}}}{10^{42} \text{ ergs s}^{-1}} \right)^{3/5} \left( \frac{T_{\text{obt}}}{64 \text{ ks}} \right)^{-2/5}. \end{aligned} \quad (25)$$

Combining Eqs.(23) and (25), we obtain  $\alpha \approx 0.01$  for the  $\beta$ -disk model.

5. *SMO nature.* In the literature, a stellar mass black hole (sBH) has been also discussed as another possibility of the SMO. In this case, the influence radius within which the gas in the disk is shocked is the accretion radius of the sBH rather than its geometrical size. To produce sufficiently energetic flares, the sBH mass has to be  $m \gtrsim 30 M_{\odot}$  and the sBH

$\Theta$	$\pi(\Theta, \mathcal{H}_1)$	$\pi(\Theta, \mathcal{H}_0)$
$p [M_\bullet]$	$\log \mathcal{U}[50, 500]$	
$e$	$\mathcal{U}[0, 0.9]$	
$\cos(\theta_{\min})$	$\mathcal{U}[0, 1]$	
$\chi_{r0}$	$\mathcal{U}[0, 2\pi]$	
$\chi_{\theta 0}$	$\mathcal{U}[0, 2\pi]$	
$\phi$	$\mathcal{U}[0, 2\pi]$	
$T_{\text{obt}} [\text{ks}]$	$\mathcal{U}[60, 70]$	
$a$	$\mathcal{U}[0, 1]$	
$\theta_{\text{obs}}$	$\mathcal{U}[0, \pi/2]$	
$\sigma_{\text{sys}} [\text{ks}]$	$\mathcal{U}[0, 500]$	
$\dot{T}_{\text{obt}} [\times 10^{-5}]$	$\mathcal{U}[-10, -0.1]$	None

TABLE I. Priors used for the orbital parameter inference of GSN 069 EMRI. Entries left blank in the  $\pi(\Theta, \mathcal{H}_0)$  column indicate that the same prior values from the  $\pi(\Theta, \mathcal{H}_1)$  column are imposed.

orbit has to be close to the accretion disk with a small inclination angle  $\iota_{\text{sd}} \lesssim 0.1$  [32]. According to Eq. (21), the sBH interpretation favors a low radiation efficiency

$$\eta_{\text{QPE}} \approx 0.3\% \times \left( \frac{m}{30M_\odot} \right)^{-1}, \quad (26)$$

which seems too low for either radiation from shocked gas or radiation from gas accretion by the sBH.

In the case of a sBH, the orbital energy loss per collision due to dynamical friction is estimated as (paper I)

$$\begin{aligned} \delta E_{\text{sBH}} &= 4\pi \ln \Lambda \frac{G^2 m^2}{v_{\text{rel}}^2} \frac{\Sigma}{\sin(\iota_{\text{sd}})}, \\ &\approx 6 \times 10^{46} \text{ergs} \left( \frac{\ln \Lambda}{10} \right) \Sigma_5 m_{30}^2 r_{300} \left( \frac{\sin \iota_{\text{sd}}}{0.1} \right)^{-3}, \end{aligned} \quad (27)$$

where  $\ln \Lambda$  is the Coulomb logarithm,  $m_{30} := m/30M_\odot$ . Equating  $\delta E_{\text{sBH}}$  to  $E_{\text{col}}$  inferred from the orbital decay rate in Eq. (20), we obtain a dense accretion disk with surface density

$$\Sigma_5 = 33_{-7}^{+7} \left( \frac{\ln \Lambda}{10} \right)^{-1} m_{30}^{-1} r_{300}^{-1} \left( \frac{\sin \iota_{\text{sd}}}{0.1} \right)^3, \quad (28)$$

at 2- $\sigma$  confidence level, which can be accommodated in an  $\alpha$ -disk with a low viscosity  $\alpha \approx 0.01$  [Eq. (24)], but seems hard to fit in a  $\beta$ -disk with a reasonable viscosity coefficient [Eq. (25)].

## B. eRO-QPE2

In paper II, we analyzed three public XMM-Newton observations of eRO-QPE2 at that time: XMM1 (2020-08-06), XMM2 (2022-02-06) and XMM3 (2022-06-21). We noticed a clear decreasing trend of the apparent orbital period from approximately 17.5 ks in XMM1 to 16.4 ks in XMM2 and 3. More observations have been done on eRO-QPE2, one of which, XMM4 (2023-12-08), is recently publicly available. Surprisingly, there is little decay in the orbital period between XMM3 and XMM4 (Fig. 2 in Ref. [28]).

$\Theta$	$\pi(\Theta, \mathcal{H}_2)$	$\pi(\Theta, \mathcal{H}_1)$	$\pi(\Theta, \mathcal{H}_0)$
$p [M_\bullet]$	$\log \mathcal{U}[10, 1000]$		
$e$	$\mathcal{U}[0, 0.9]$		
$\cos(\theta_{\min})$	$\mathcal{U}[0, 1]$		
$q_{r,\text{ini}}$	$\mathcal{U}[0, 2\pi]$		
$q_{z,\text{ini}}$	$\mathcal{U}[0, 2\pi]$		
$q_{\phi,\text{ini}}$	$\mathcal{U}[0, 2\pi]$		
$T_{\text{obt}} [\text{ks}]$	$\mathcal{U}[14.4, 25]$	$\mathcal{U}[10, 25]$	$\mathcal{U}[10, 25]$
$a$	$\mathcal{U}[0, 1]$		
$\theta_{\text{obs}}$	$\mathcal{U}[0, \pi/2]$		
$\alpha_{\text{ini}}$	$\mathcal{U}[0, 2\pi]$		None
$\tau_{\text{p}} [\text{days}]$	$\mathcal{U}[0.5, 50]$		None
$\beta_{\text{ini}}$	$\mathcal{U}[0, \pi/2]$		None
$\dot{T}_{\text{obt,max}}$	$\mathcal{U}[-10^{-4}, -10^{-6}]$	None	None
$\sigma_{\text{sys}} [\text{ks}]$	$\mathcal{U}[0, 2]$		

TABLE II. Same to Table I except for eRO-QPE2. The tighter prior range of  $T_{\text{obt}}$  in  $\mathcal{H}_2$  is for sampling efficiency.

To understand the whole evolution history of the apparent orbital period, we consider two different possibilities: 1) a fast disk alignment hypothesis ( $\mathcal{H}_1 = \mathcal{H}_{\text{e0}} + \mathcal{H}_{\text{df}}$ ), where the apparent long orbital period in XMM1 is a result of a misaligned disk precessing in the same direction to the SMO orbital angular momentum direction, and the apparent orbital period in XMM2-4 restore a constant value after the disk alignment completes; 2) a hypothesis of a forced EMRI trajectory and a precessing disk ( $\mathcal{H}_2 = \mathcal{H}_{\text{e1}} + \mathcal{H}_{\text{ds}}$ ), where the nonuniform orbital decay is modulated by the angle between the SMO orbital plane and the disk plane as formulated in Eq. (9) [28]. For comparison, we also consider the vanilla hypothesis ( $\mathcal{H}_0 = \mathcal{H}_{\text{e0}} + \mathcal{H}_{\text{d0}}$ ) as in the analysis of GSN 069.

In Table II, we show the priors of model parameters used for orbital analyses in  $\mathcal{H}_0$ ,  $\mathcal{H}_1$  and  $\mathcal{H}_2$ . In Fig. 2, the best-fit EMRI trajectories of the three hypotheses are displayed together with the QPE light curves, with orbital parameters  $p = 370 M_\bullet$ ,  $e = 0.00$ ,  $T_{\text{obt}} = 17.1$  ks ( $\mathcal{H}_0$ ), and  $p = 514 M_\bullet$ ,  $e = 0.04$ ,  $T_{\text{obt}} = 16.46$  ks,  $\tau_{\text{p}} = 3$  d ( $\mathcal{H}_1$ ) and  $p = 260 M_\bullet$ ,  $e = 0.02$ ,  $T_{\text{obt}} = 17.3$  ks,  $\tau_{\text{p}} = 9$  d,  $\dot{T}_{\text{obt,max}} = -2.0 \times 10^{-5}$  ( $\mathcal{H}_2$ ). In  $\mathcal{H}_2$ , the non-uniform orbital decay rate  $\dot{T}_{\text{obt}}$  is proportional to  $z_{\text{disk}}(t) \approx p \sin \iota_{\text{sd}}(t)$  and the best-fit trajectory favors a low  $\dot{T}_{\text{obt}}$  around XMM3. In  $\mathcal{H}_1$ , the apparent non-uniform orbital decay rate is the result of the disk alignment process. The best-fit trajectory favors a fast disk alignment, where the apparent orbital period is longer than the true period during XMM1 due to the disk precession, and converges to the true period after the disk alignment (XMM2-4).

The posterior corner plots of all model parameters are shown in Fig. 7, Fig. 8 and Fig. 9, respectively, where the orbital parameters are constrained as

$$\begin{aligned} p &= 492_{-310}^{+386} M_\bullet, \\ e &= 0.03_{-0.03}^{+0.06}, \quad (\mathcal{H}_0) \\ T_{\text{obt}} &= 17.1_{-0.2}^{+0.2} \text{ks}, \end{aligned} \quad (29)$$

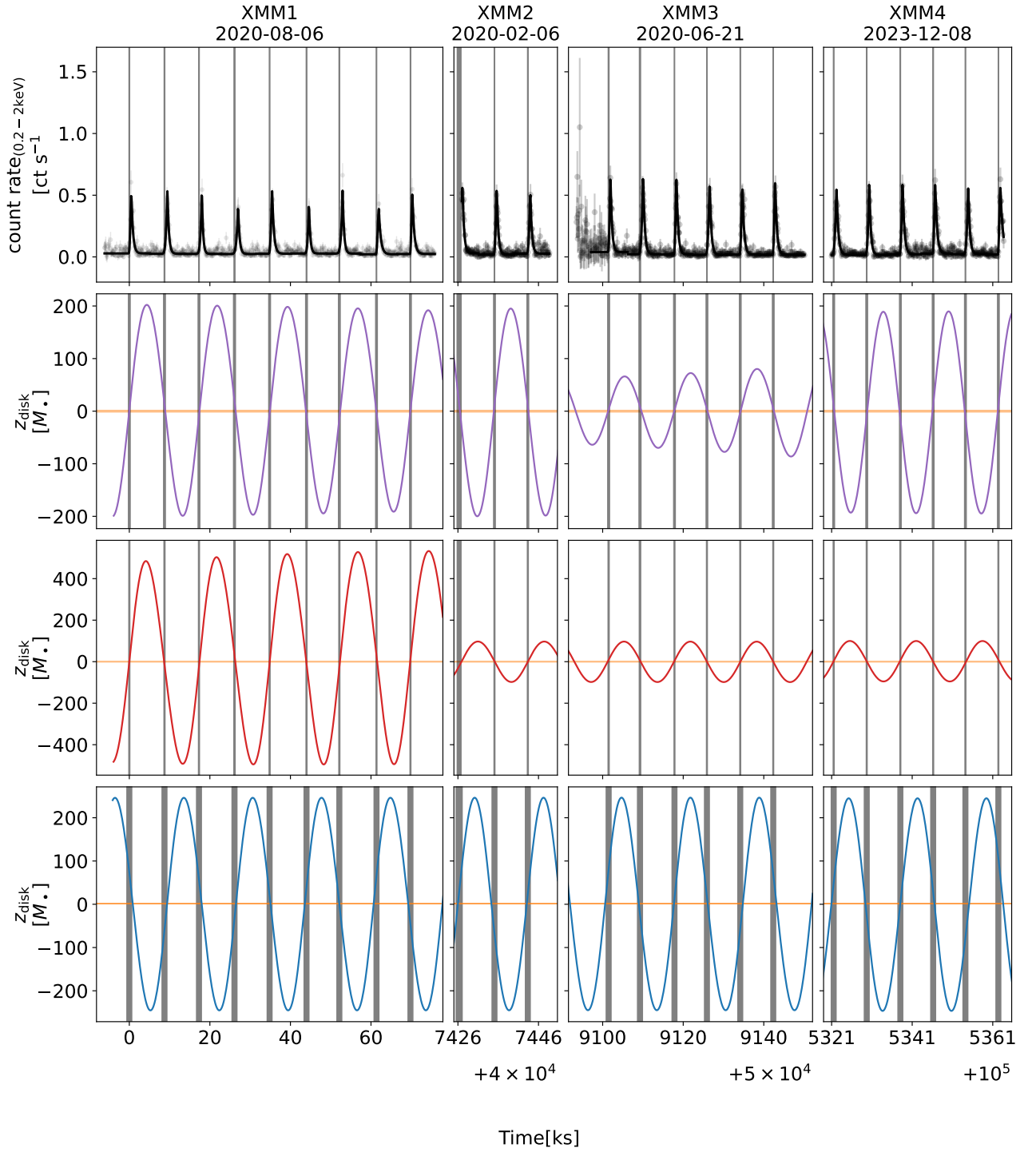


FIG. 2. Same to Fig. 1 except for eRO-QPE2. Purple: Forced EMRI + slow alignment hypothesis ( $\mathcal{H}_2$ ); Red: fast alignment hypothesis ( $\mathcal{H}_1$ ); Blue: vanilla hypothesis ( $\mathcal{H}_0$ ).



and

$$\begin{aligned} p &= 616_{-260}^{+275} M_{\bullet}, \\ e &= 0.01_{-0.01}^{+0.01}, \quad (\mathcal{H}_1) \\ T_{\text{obt}} &= 16.46_{-0.00}^{+0.04} \text{ ks}, \\ \tau_p &= 3.1_{-0.3}^{+0.3} \text{ days}, \end{aligned} \quad (30)$$

and

$$\begin{aligned} p &= 430_{-210}^{+372} M_{\bullet}, \\ e &= 0.02_{-0.01}^{+0.02}, \\ T_{\text{obt}} &= 17.4_{-0.1}^{+0.1} \text{ ks}, \quad (\mathcal{H}_2) \\ \tau_p &= 13_{-8}^{+26} \text{ days}, \\ \dot{T}_{\text{obt,max}} &= -1.8_{-0.8}^{+0.6} \times 10^{-5}, \end{aligned} \quad (31)$$

at  $2\text{-}\sigma$  confidence level. The log Bayes factors between the three hypotheses are found to be

$$\begin{aligned} \log \mathcal{B}_0^1 &= 16.0 \pm 0.2, \\ \log \mathcal{B}_0^2 &= 14.7 \pm 0.2. \end{aligned} \quad (32)$$

Comparing with the vanilla hypothesis  $\mathcal{H}_0$ ,  $\mathcal{H}_1$  and  $\mathcal{H}_2$  are nearly equally favored, where the apparent orbital period decay is the result of disk alignment process in  $\mathcal{H}_1$  and is the true orbital decay in  $\mathcal{H}_2$ . In either case, the disk precession is required. With the current data, we find the constraints on the SMBH mass as

$$\begin{aligned} \log_{10}(M_{\bullet}/M_{\odot}) &= 4.5_{-0.2}^{+0.4}, \quad (\mathcal{H}_1) \\ \log_{10}(M_{\bullet}/M_{\odot}) &= 4.8_{-0.4}^{+0.4}, \quad (\mathcal{H}_2) \end{aligned} \quad (33)$$

at  $2\text{-}\sigma$  confidence level. These constraints are consistent with the value  $\log_{10}(M_{\bullet}/M_{\odot}) = 4.96 \pm 1.1$  ( $2\text{-}\sigma$ ) inferred from the  $M_{\bullet} - \sigma_{\star}$  relation [14]. As a conservative estimate of the SMBH mass constrained by the QPE timing, we consider the two hypotheses are equally weighted, as a result, we obtain

$$\log_{10}(M_{\bullet}/M_{\odot}) = 4.7 \pm 0.5, \quad (\mathcal{H}_1 \text{ or } \mathcal{H}_2) \quad (34)$$

at  $2\text{-}\sigma$  confidence level. It is interesting to note that the SMBH of eRO-QPE2 is on the edge of intermediate mass BHs. With longer monitoring of eRO-QPE2, we expect to distinguish the two hypotheses and further pin down the SMBH mass.

#### IV. SUMMARY AND DISCUSSIONS

In this work, we have extended the previous orbital analyses of QPE timing by including the EMRI orbital period decay due to collisions with the accretion disk and the disk precession/alignment if the disk is initially misaligned. We have applied this generalized orbital analysis to GSN 069 and eRO-QPE2, the two most stable QPE sources so far.

Regarding GSN 069, we find clear Bayesian evidence for the non-zero orbital period decay rate  $\dot{T}_{\text{obt}}$  [Eq. (15)], along with tight constraints on the SMBH mass  $M_{\bullet}$ , the orbital size  $p$  and the orbital eccentricity  $e$ . From these constraints, we

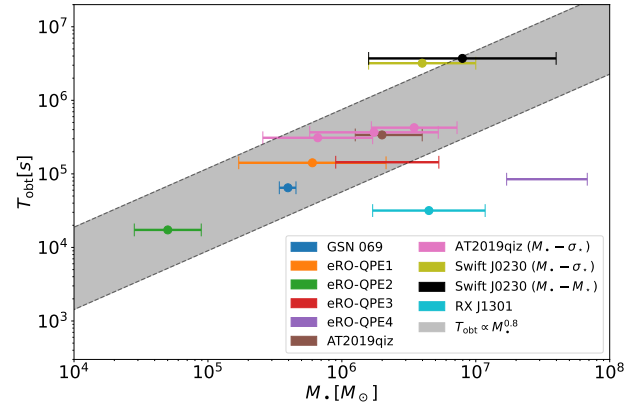


FIG. 3. Population properties of QPE sources: orbital periods  $T_{\text{obt}}$  v.s. SMBH masses  $M_{\bullet}$ , where error bars in the diagram represent  $1\text{-}\sigma$  uncertainties. We have shown 4 mass measurements of AT2019qiz from TDE disk modeling and from 3 widely used  $M_{\bullet} - \sigma_{\star}$  relations [12, 69], and 2 mass measurements of Swift J0230 from two different host galaxy scaling relations [10].

can directly measure the EMRI orbital energy loss as crossing the accretion disk  $E_{\text{col}}$ , and the QPE radiation efficiency  $\eta_{\text{QPE}}$  in combination with the QPE light curves. We find  $\eta_{\text{QPE}} \approx 10\%(M_{\odot}/m)$  in the case of GSN 069. This radiation efficiency looks reasonable for a normal star with  $m \approx 1M_{\odot}$  as the secondary object but seems to be too low for a sBH with  $m \gtrsim 30M_{\odot}$ . A firm conclusion on the nature of the SMO based on the measured QPE radiation efficiency requires detailed analysis of the QPE radiation processes, which we will report in a separate paper.

Regarding eRO-QPE2, the authors of Ref. [28] already noticed its non-uniform orbital decay and interpreted this behavior as a result of the disk precession [Eq. (9)]. In this work, we consider another possibility: the apparent non-uniform orbital decay is a result of the disk alignment process. In the framework of Bayesian analysis on the QPE timing, we find the two hypotheses are nearly equally favored by the current data. The two hypotheses predict distinct future evolution of the EMRI orbital period: the former predicts a periodic change in  $\dot{T}_{\text{obt}}$ , while the latter predicts a constant  $\dot{T}_{\text{obt}}$ . The two different predictions should be able to be distinguished by the 2024 observations of XMM-Newton. We will do a follow-up analysis when the 2024 data are released for public use.

With the generalized QPE timing model, we incorporate different observations spanning a long time into a single orbital analysis and obtain tighter constraints on the EMRI orbital parameters. The tighter constraints of the orbital eccentricities further confirm the conclusion on the EMRI formation history in papers I and II: they are consistent with the wet channel prediction [38–46], but incompatible with either the dry channel [47–52] or the Hills channel [53, 54].

Tighter constraints of the orbital parameters also open the possibility of accurately quantifying the population statistics of QPE sources. In Fig. 3, we show the orbital periods  $T_{\text{obt}}$  and the SMBH masses  $M_{\bullet}$  of 8 QPE sources, where the SMBH masses of GSN 069 and eRO-QPE2 are inferred from the QPE

timing as shown in this paper [Eqs. (19,34)], and others are from host galaxy scaling relations [10, 11, 14, 69] or TDE disk modeling [12]. Similar diagram could be also be found in Refs. [10, 12], where no clear evidence for the  $T_{\text{obt}} - M_{\bullet}$  correlation was found. With better constraints of the SMBH masses of GSN 069 and eRO-QPE2, we find a likely correlation  $T_{\text{obt}} \propto M_{\bullet}^n$  with  $n \approx 0.8$ , excluding RX J1301 and eRO-QPE4. These two QPE sources are exceptional in their high orbital eccentricities (see [2, 30, 32] for detailed analyses of RX J1301 and [11] for the light curves of eRO-QPE4 which shows a large difference between the long recurrence times and the short ones). Therefore, an interesting implication of this diagram is that there are two populations of QPEs sourced by low-eccentricity and high-eccentricity EMRIs, respectively. The low-eccentricity population follows a scaling  $T_{\text{obt}} \propto M_{\bullet}^{0.8}$ , while it is unclear whether a similar correlation exists in the high-eccentricity population due to the limited number of sources. If the dichotomy is confirmed with more QPE sources to be discovered in the future, it will be a smoking-gun signature of multiple EMRI formation channels and the correlation(s) further shed light on the physical processes functioning in different channels.

*Note added:* As we were finishing this paper, Ref. [25] appeared on arXiv, where the authors did a detailed Observed minus Calculated (O-C) analysis of the GSN 069 QPE timing, and found evidence for orbital period decay and for super-orbital modulation on tens of days. They interpreted the mod-

ulation as evidence for disk precession or a sub-milliparsec SMBH binary. The orbital period decay rate they found is consistent with our result. But we found no evidence for disk precession (see the red line in Fig. 1 for a reasonable fit to the data without invoking disk precession and the featureless residuals in Fig. 4). The discrepancy may come from different models and different analysis methods used. We fit the QPE timing data with forced EMRI trajectories in the Kerr space-time, and all the data interpretation are done in the Bayesian analysis framework. The authors of Ref. [25] adopted a simple phenomenological model instead and interpreted the data in a pictorial approach. More importantly, their best-fit sinusoidal modulation period  $P_{\text{mod}} \sim 19$  d is coincident with 1/4 times the median value of the EMRI apsidal precession period in our orbital analysis,  $T_{\text{prec}}/4 = 25T_{\text{obt}} = 18.7$  d [Eq. (15)]. This coincidence indicates that the modulation with  $P_{\text{mod}} \sim 19$  d found in their O-C analysis is actually evidence for the EMRI apsidal precession.

## ACKNOWLEDGMENTS

We thank Ning Jiang and Shifeng Huang for valuable discussions. The computations in this paper were run on the Siyuan-I cluster supported by the Center for High Performance Computing at Shanghai Jiao Tong University.

- 
- [1] Cong Zhou, Lei Huang, Kangrou Guo, Ya-Ping Li, and Zhen Pan, “Probing orbits of stellar mass objects deep in galactic nuclei with quasiperiodic eruptions,” *Phys. Rev. D* **109**, 103031 (2024), arXiv:2401.11190 [astro-ph.HE].
- [2] Cong Zhou, Binyu Zhong, Yuhe Zeng, Lei Huang, and Zhen Pan, “Probing orbits of stellar mass objects deep in galactic nuclei with quasiperiodic eruptions. II. Population analysis,” *Phys. Rev. D* **110**, 083019 (2024), arXiv:2405.06429 [astro-ph.HE].
- [3] Luming Sun, Xinwen Shu, and Tinggui Wang, “RX J1301.9+2747: A Highly Variable Seyfert Galaxy with Extremely Soft X-Ray Emission,” *Astrophys. J.* **768**, 167 (2013), arXiv:1304.3244 [astro-ph.GA].
- [4] G. Miniutti, R. D. Saxton, M. Giustini, K. D. Alexander, R. P. Fender, I. Heywood, I. Monageng, M. Coriat, A. K. Tzioumis, A. M. Read, C. Knigge, P. Gandhi, M. L. Pretorius, and B. Agís-González, “Nine-hour X-ray quasi-periodic eruptions from a low-mass black hole galactic nucleus,” *Nature (London)* **573**, 381–384 (2019), arXiv:1909.04693 [astro-ph.HE].
- [5] Margherita Giustini, Giovanni Miniutti, and Richard D. Saxton, “X-ray quasi-periodic eruptions from the galactic nucleus of RX J1301.9+2747,” *Astronomy&Astrophysics* **636**, L2 (2020), arXiv:2002.08967 [astro-ph.HE].
- [6] R. Arcodia, A. Merloni, K. Nandra, J. Buchner, M. Salvato, D. Pasham, R. Remillard, J. Comparat, G. Lamer, G. Ponti, A. Malyali, J. Wolf, Z. Arzoumanian, D. Bogensberger, D. A. H. Buckley, K. Gendreau, M. Gromadzki, E. Kara, M. Krumpe, C. Markwardt, M. E. Ramos-Ceja, A. Rau, M. Schramm, and A. Schwobe, “X-ray quasi-periodic eruptions from two previously quiescent galaxies,” *Nature (London)* **592**, 704–707 (2021), arXiv:2104.13388 [astro-ph.HE].
- [7] R. Arcodia, G. Miniutti, G. Ponti, J. Buchner, M. Giustini, A. Merloni, K. Nandra, F. Vincentelli, E. Kara, M. Salvato, and D. Pasham, “The complex time and energy evolution of quasiperiodic eruptions in eRO-QPE1,” *Astronomy&Astrophysics* **662**, A49 (2022), arXiv:2203.11939 [astro-ph.HE].
- [8] Joheen Chakraborty, Erin Kara, Megan Masterson, Margherita Giustini, Giovanni Miniutti, and Richard Saxton, “Possible X-Ray Quasi-periodic Eruptions in a Tidal Disruption Event Candidate,” *Astroph.J.Lett.* **921**, L40 (2021), arXiv:2110.10786 [astro-ph.HE].
- [9] P. A. Evans, C. J. Nixon, S. Campana, P. Charalampopoulos, D. A. Perley, A. A. Breeveld, K. L. Page, S. R. Oates, R. A. J. Eyles-Ferris, D. B. Malesani, L. Izzo, M. R. Goad, P. T. O’Brien, J. P. Osborne, and B. Sbarufatti, “Monthly quasi-periodic eruptions from repeated stellar disruption by a massive black hole,” *Nature Astronomy* **7**, 1368–1375 (2023), arXiv:2309.02500 [astro-ph.HE].
- [10] Muryel Guolo, Dheeraj R. Pasham, Michal Zajaček, Eric R. Coughlin, Suvi Gezari, Petra Suková, Thomas Wevers, Vojtěch Witzany, Francesco Tombesi, Sjoert van Velzen, Kate D. Alexander, Yuhan Yao, Riccardo Arcodia, Vladimír Karas, James C. A. Miller-Jones, Ronald Remillard, Keith Gendreau, and Elizabeth C. Ferrara, “X-ray eruptions every 22 days from the nucleus of a nearby galaxy,” *Nature Astronomy* (2024), 10.1038/s41550-023-02178-4, arXiv:2309.03011 [astro-ph.HE].
- [11] R. Arcodia, Z. Liu, A. Merloni, A. Malyali, A. Rau, J. Chakraborty, A. Goodwin, D. Buckley, J. Brink, M. Gro-

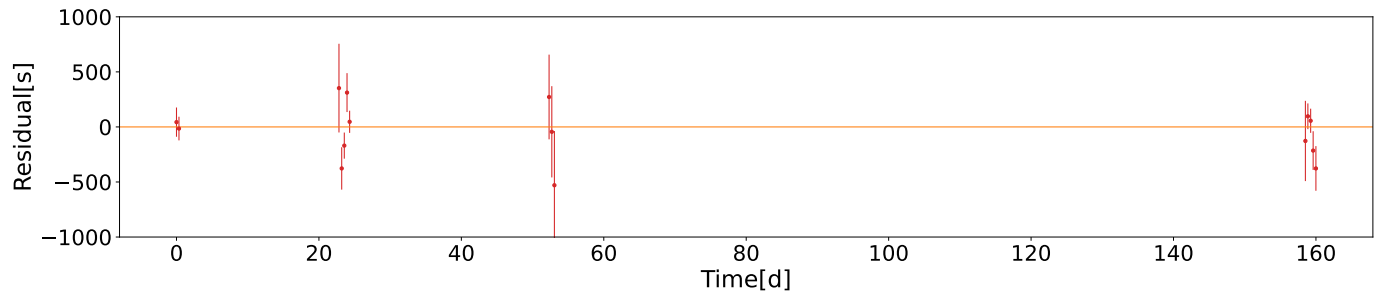


FIG. 4. Residuals of the best-fit QPE timing model with  $\mathcal{H}_1$  for GSN 069, i.e.  $t_{\text{obs}}^{(k)} - t_0^{(k)}$ , where error bars represent  $1-\sigma$  uncertainties.

- madzki, Z. Arzoumanian, J. Buchner, E. Kara, K. Nandra, G. Ponti, M. Salvato, G. Anderson, P. Baldini, I. Grotova, M. Krumpke, C. Maitra, J. C. A. Miller-Jones, and M. E. Ramos-Ceja, “The more the merrier: SRG/eROSITA discovers two further galaxies showing X-ray quasi-periodic eruptions,” *arXiv e-prints*, [arXiv:2401.17275 \(2024\)](#), [arXiv:2401.17275 \[astro-ph.HE\]](#).
- [12] M. Nicholl, D. R. Pasham, A. Mummery, M. Guolo, K. Gendreau, G. C. Dewangan, E. C. Ferrara, R. Remillard, C. Bonnerot, J. Chakraborty, A. Hajela, V. S. Dhillon, A. F. Gillan, J. Greenwood, M. E. Huber, A. Janiuk, G. Salvesen, S. van Velzen, A. Aamer, K. D. Alexander, C. R. Angus, Z. Arzoumanian, K. Auchettl, E. Berger, T. de Boer, Y. Cendes, K. C. Chambers, T. W. Chen, R. Chornock, M. D. Fulton, H. Gao, J. H. Gillanders, S. Gomez, B. P. Gompertz, A. C. Fabian, J. Herman, A. Ingram, E. Kara, T. Laskar, A. Lawrence, C. C. Lin, T. B. Lowe, E. A. Magnier, R. Margutti, S. L. McGee, P. Minguez, T. Moore, E. Nathan, S. R. Oates, K. C. Patra, P. Ramsden, V. Ravi, E. J. Ridley, X. Sheng, S. J. Smartt, K. W. Smith, S. Srivastav, R. Stein, H. F. Stevance, S. G. D. Turner, R. J. Wainscoat, J. Weston, T. Wevers, and D. R. Young, “Quasi-periodic x-ray eruptions years after a nearby tidal disruption event,” (2024), [arXiv:2409.02181 \[astro-ph.HE\]](#).
- [13] Xinwen Shu, Tinggui Wang, Ning Jiang, Junxian Wang, Luming Sun, and Hongyan Zhou, “Central Engine and Host Galaxy of RXJ 1301.9+2747: A Multiwavelength View of a Low-mass Black Hole Active Galactic Nuclei with Ultra-soft X-ray Emission,” *Astrophys. J.* **837**, 3 (2017), [arXiv:1704.02886 \[astro-ph.HE\]](#).
- [14] T. Wevers, D. R. Pasham, P. Jalan, S. Rakshit, and R. Arcodia, “Host galaxy properties of quasi-periodically erupting X-ray sources,” *Astronomy&Astrophysics* **659**, L2 (2022), [arXiv:2201.11751 \[astro-ph.HE\]](#).
- [15] G. Miniutti, M. Giustini, R. Arcodia, R. D. Saxton, J. Chakraborty, A. M. Read, and E. Kara, “Alive and kicking: A new QPE phase in GSN 069 revealing a quiescent luminosity threshold for QPEs,” *Astronomy&Astrophysics* **674**, L1 (2023), [arXiv:2305.09717 \[astro-ph.HE\]](#).
- [16] Thomas Wevers and K. Decker French, “Extended Emission-line Regions in Poststarburst Galaxies Hosting Tidal Disruption Events,” *Astrophys. J. Lett.* **969**, L17 (2024), [arXiv:2406.02674 \[astro-ph.GA\]](#).
- [17] T. Wevers *et al.*, “X-Ray Quasi-periodic Eruptions and Tidal Disruption Events Prefer Similar Host Galaxies,” *Astrophys. J. Lett.* **970**, L23 (2024), [arXiv:2406.02678 \[astro-ph.HE\]](#).
- [18] Olivier Gilbert, John J. Ruan, Michael Eracleous, Daryl Haggard, and Jessie C. Runnoe, “A Host Galaxy Morphology Link Between Quasi-Periodic Eruptions and Tidal Disruption Events,” (2024), [arXiv:2409.10486 \[astro-ph.HE\]](#).
- [19] X. W. Shu, S. S. Wang, L. M. Dou, N. Jiang, J. X. Wang, and T. G. Wang, “A Long Decay of X-Ray Flux and Spectral Evolution in the Supersoft Active Galactic Nucleus GSN 069,” *Astrophys. J. Lett.* **857**, L16 (2018), [arXiv:1809.00319 \[astro-ph.HE\]](#).
- [20] Zhenfeng Sheng, Tinggui Wang, Gary Ferland, Xinwen Shu, Chenwei Yang, Ning Jiang, and Yang Chen, “Evidence of a Tidal-disruption Event in GSN 069 from the Abnormal Carbon and Nitrogen Abundance Ratio,” *Astrophys. J. Lett.* **920**, L25 (2021), [arXiv:2109.01683 \[astro-ph.GA\]](#).
- [21] E. Quintin, N. A. Webb, S. Guillot, G. Miniutti, E. S. Kamoun, M. Giustini, R. Arcodia, G. Soucail, N. Clerc, R. Amato, and C. B. Markwardt, “Tormund’s return: Hints of quasi-periodic eruption features from a recent optical tidal disruption event,” *Astronomy&Astrophysics* **675**, A152 (2023), [arXiv:2306.00438 \[astro-ph.HE\]](#).
- [22] Sergei Bykov, Marat Gilfanov, Rashid Sunyaev, and Pavel Medvedev, “Further evidence of Quasiperiodic Eruptions in a tidal disruption event AT2019vcb by SRG/eROSITA,” (2024), [arXiv:2409.16908 \[astro-ph.HE\]](#).
- [23] K. Decker French, Nicholas Earl, Annemarie B. Novack, Bhavya Pardasani, Vismaya R. Pillai, Akshat Tripathi, and Margaret E. Verrico, “Fading AGNs in Poststarburst Galaxies,” *Astrophys. J.* **950**, 153 (2023).
- [24] G. Miniutti, M. Giustini, R. Arcodia, R. D. Saxton, A. M. Read, S. Bianchi, and K. D. Alexander, “Repeating tidal disruptions in GSN 069: Long-term evolution and constraints on quasi-periodic eruptions’ models,” *Astronomy&Astrophysics* **670**, A93 (2023), [arXiv:2207.07511 \[astro-ph.HE\]](#).
- [25] Giovanni Miniutti *et al.*, “Eppur si muove: Evidence of disc precession or a sub-milliparsec SMBH binary in the QPE-emitting galaxy GSN 069,” (2024), [arXiv:2411.13460 \[astro-ph.HE\]](#).
- [26] Dheeraj R. Pasham, Eric R. Coughlin, Michal Zajacek, Itai Linial, Petra Sukova, Christopher J. Nixon, Agnieszka Janiuk, Marzena Sniegowska, Wojtech Witzany, Vladimir Karas, M. Krumpke, Diego Altamirano, Thomas Wevers, and Riccardo Arcodia, “Alive but Barely Kicking: News from 3+ years of Swift and XMM-Newton X-ray Monitoring of Quasi-Periodic Eruptions from eRO-QPE1,” *arXiv e-prints*, [arXiv:2402.09690 \(2024\)](#), [arXiv:2402.09690 \[astro-ph.HE\]](#).
- [27] Joheen Chakraborty, Riccardo Arcodia, Erin Kara, Giovanni Miniutti, Margherita Giustini, Alexandra J. Tetarenko, Lauren Rhodes, Alessia Franchini, Matteo Bonetti, Kevin B. Burdge, Adelle J. Goodwin, Thomas J. Maccarone, Andrea Merloni, Gabriele Ponti, Ronald A. Remillard, and Richard D. Saxton, “Testing EMRI models for Quasi-Periodic Eruptions with 3.5 years of monitoring eRO-QPE1,” *arXiv e-prints*,

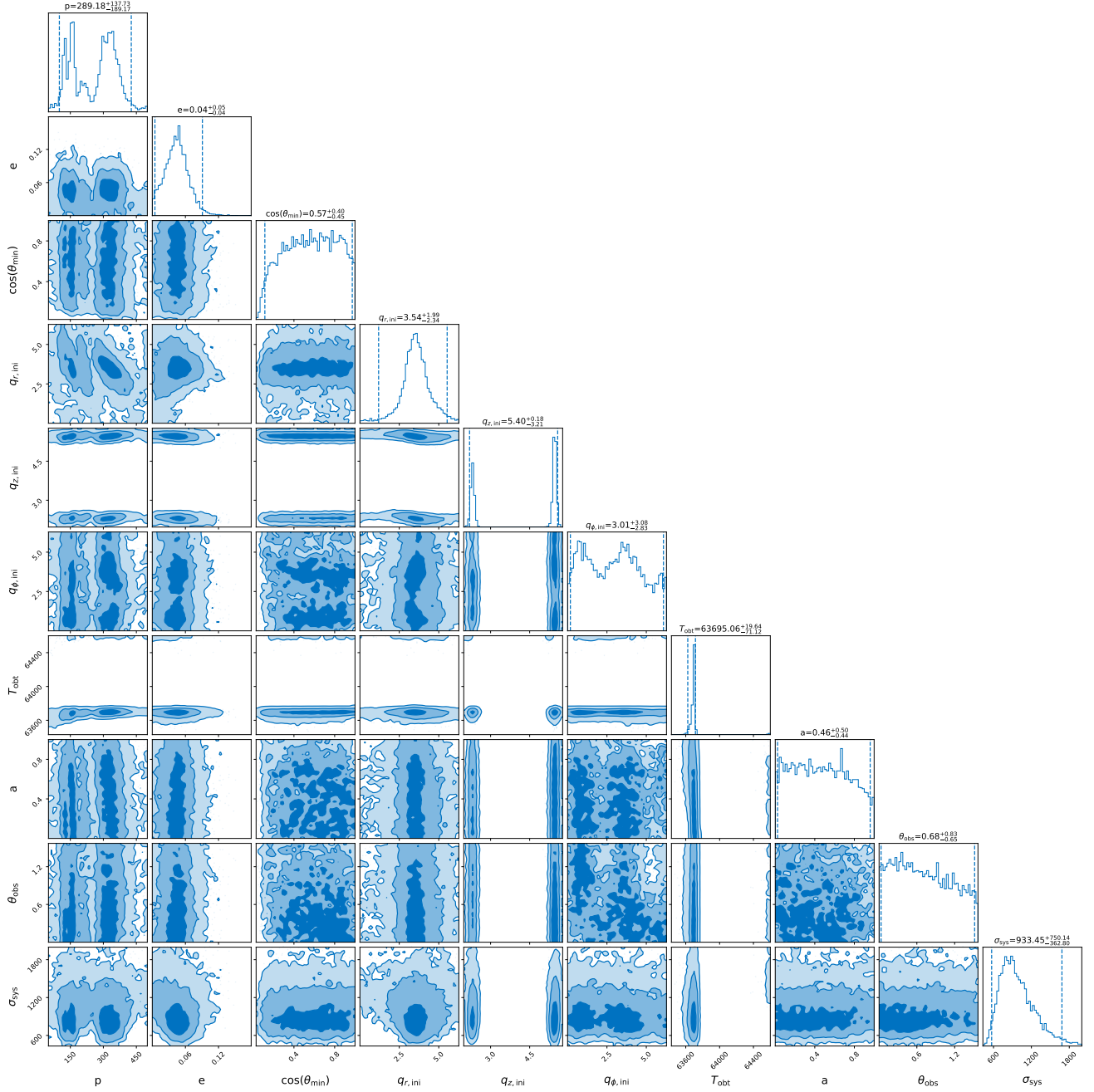


FIG. 5. The posterior corner plot of model parameters for GSN 069 with the vanilla hypothesis ( $\mathcal{H}_0$ ) :  $p[M_\bullet]$ ,  $e$ ,  $\cos \theta_{\min}$ ,  $q_{r,\text{ini}}$ ,  $q_{z,\text{ini}}$ ,  $q_{\phi,\text{ini}}$ ,  $T_{\text{obs}}[\text{sec}]$ ,  $a$ ,  $\theta_{\text{obs}}$ ,  $\sigma_{\text{sys}}[\text{sec}]$ , where each pair of vertical lines denotes the  $2\text{-}\sigma$  confidence level.

- [arXiv:2402.08722 \(2024\)](#), [arXiv:2402.08722 \[astro-ph.HE\]](#).
- [28] R. Arcodia *et al.*, “Ticking away: the long-term X-ray timing and spectral evolution of eRO-QPE2,” (2024), [arXiv:2406.17020 \[astro-ph.HE\]](#).
- [29] Dheeraj Pasham, Shubham Kejriwal, Eric Coughlin, Vojtěch Witzany, Alvin J. K. Chua, Michal Zajaček, Thomas Wevers, and Yukta Ajay, “Alive and Strongly Kicking: Stable X-ray Quasi-Periodic Eruptions from eRO-QPE2 over 3.5 Years,” (2024), [arXiv:2411.00289 \[astro-ph.HE\]](#).
- [30] Margherita Giustini *et al.*, “Fragments of harmony amid apparent chaos: a closer look at the X-ray quasi-periodic eruptions of the galaxy RX J1301.9+2747,” (2024), [arXiv:2409.01938 \[astro-ph.HE\]](#).
- [31] Itai Linial and Brian D. Metzger, “EMRI + TDE = QPE: Periodic X-ray Flares from Star-Disk Collisions in Galactic Nuclei,” [arXiv e-prints](#), [arXiv:2303.16231 \(2023\)](#), [arXiv:2303.16231 \[astro-ph.HE\]](#).
- [32] Alessia Franchini, Matteo Bonetti, Alessandro Lupi, Giovanni Miniutti, Elisa Bortolas, Margherita Giustini, Massimo Dotti, Alberto Sesana, Riccardo Arcodia, and Taeho Ryu, “Quasi-periodic eruptions from impacts between the secondary and a rigidly precessing accretion disc in an extreme mass-ratio in-



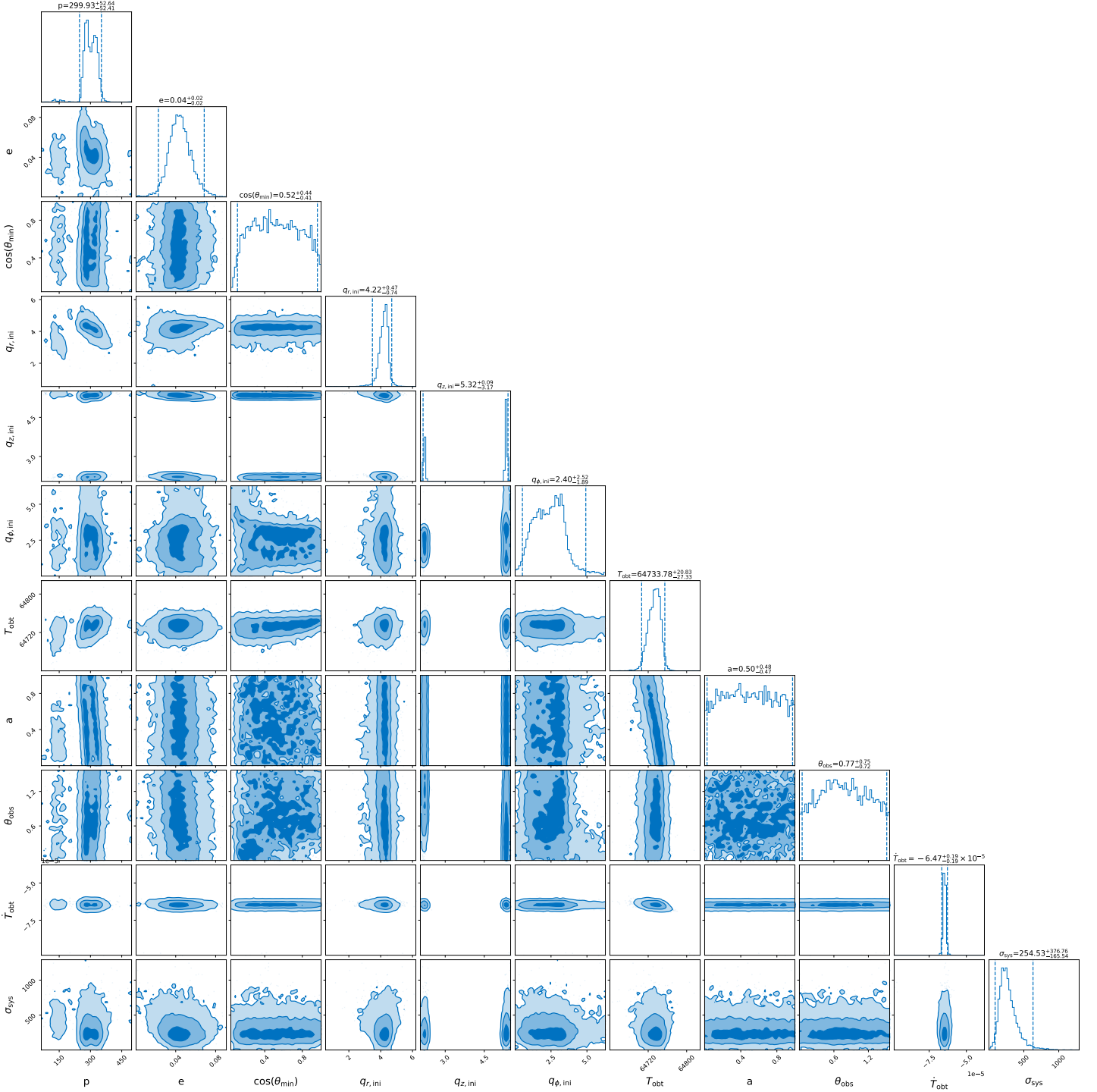


FIG. 6. The posterior corner plot of model parameters for GSN 069 with a forced EMRI + an equatorial disk hypothesis ( $\mathcal{H}_1 = \mathcal{H}_{e1} + \mathcal{H}_{d0}$ ):  $p[M_\bullet]$ ,  $e$ ,  $\cos \theta_{\min}$ ,  $q_{r,\text{ini}}$ ,  $q_{z,\text{ini}}$ ,  $q_{\phi,\text{ini}}$ ,  $T_{\text{obs}}[\text{sec}]$ ,  $a$ ,  $\theta_{\text{obs}}$ ,  $\sigma_{\text{sys}}[\text{sec}]$ , and  $\dot{T}_{\text{obs}}$ , where each pair of vertical lines denotes the  $2\text{-}\sigma$  confidence level.

- spiral system,” *Astronomy&Astrophysics* **675**, A100 (2023), [arXiv:2304.00775 \[astro-ph.HE\]](#).
- [33] Itai Linial and Brian D. Metzger, “Coupled Disk-Star Evolution in Galactic Nuclei and the Lifetimes of QPE Sources,” (2024), [arXiv:2404.12421 \[astro-ph.HE\]](#).

- [34] Philippe Z. Yao, Eliot Quataert, Yan-Fei Jiang, Wenbin Lu, and Christopher J. White, “Star-Disk Collisions: Implications for QPEs and Other Transients Near Supermassive Black Holes,” (2024), [arXiv:2407.14578 \[astro-ph.HE\]](#).
- [35] Indrek Vurm, Itai Linial, and Brian D. Metzger, “Radiation Transport Simulations of Quasi-Periodic Eruptions from Star-



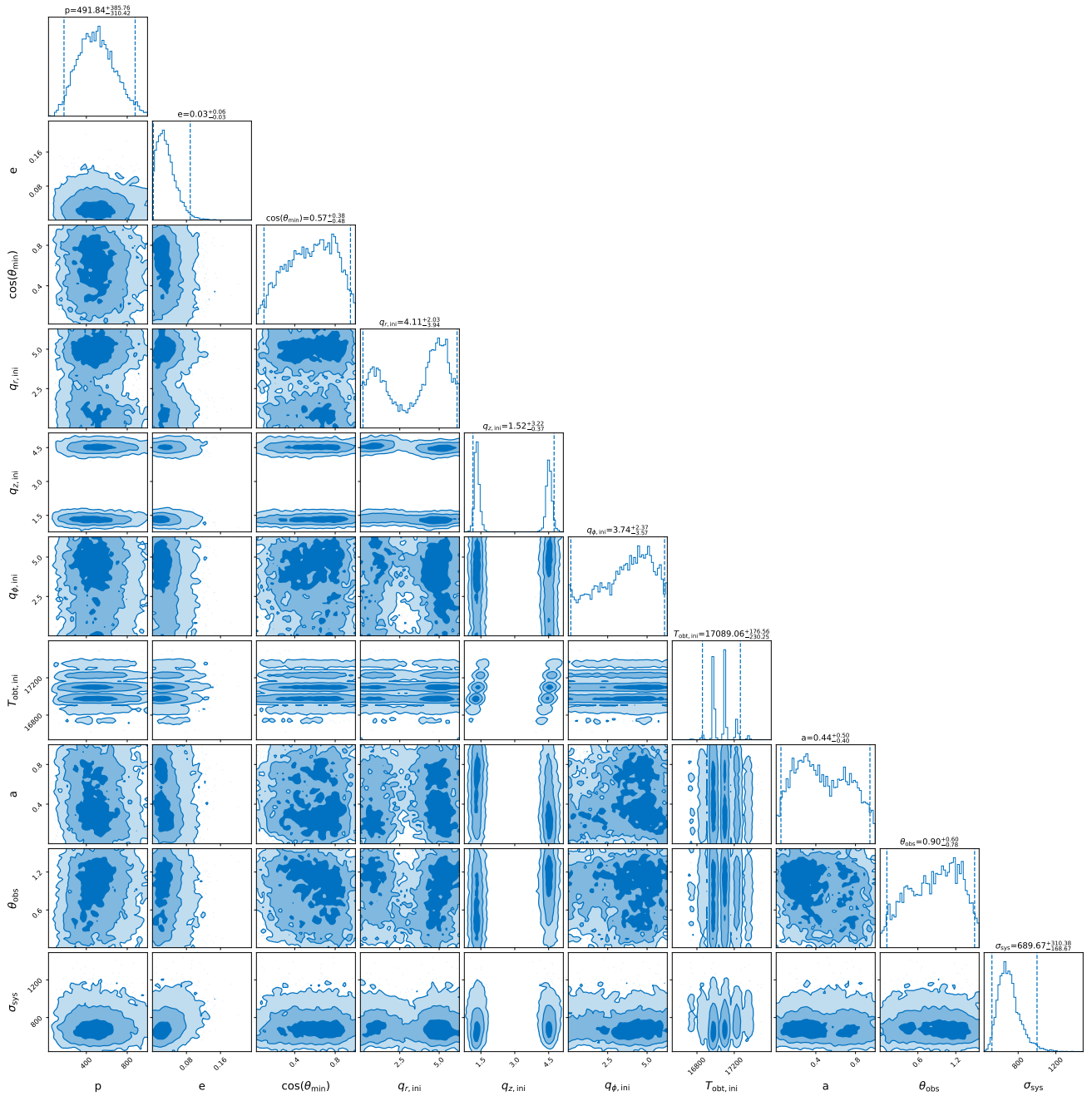


FIG. 7. Same to Fig. 5 except for eRO-QPE2.

- Disk Collisions,” (2024), [arXiv:2410.05166 \[astro-ph.HE\]](#).
- [36] R. Arcodia, A. Merloni, J. Buchner, P. Baldini, G. Ponti, A. Rau, Z. Liu, K. Nandra, and M. Salvato, “Cosmic hide and seek: the volumetric rate of X-ray quasi-periodic eruptions,” (2024), [arXiv:2403.17059 \[astro-ph.HE\]](#).
- [37] Karamveer Kaur, Barak Rom, and Re’em Sari, “Semi-Analytical Fokker Planck Models for Nuclear Star Clusters,” (2024), [arXiv:2406.07627 \[astro-ph.HE\]](#).
- [38] Günter Sigl, Jeremy Schnittman, and Alessandra Buonanno, “Gravitational-wave background from compact objects embedded in active galactic nuclei accretion disks,” *Phys. Rev. D* **75**, 024034 (2007), [arXiv:astro-ph/0610680 \[astro-ph\]](#).
- [39] Yuri Levin, “Starbursts near supermassive black holes: young stars in the Galactic Centre, and gravitational waves in LISA band,” *MNRAS* **374**, 515–524 (2007), [arXiv:astro-ph/0603583 \[astro-ph\]](#).
- [40] Zhen Pan and Huan Yang, “Formation rate of extreme mass ratio inspirals in active galactic nuclei,” *Phys. Rev. D* **103**, 103018 (2021), [arXiv:2101.09146 \[astro-ph.HE\]](#).
- [41] Zhen Pan, Zhenwei Lyu, and Huan Yang, “Wet extreme mass ratio inspirals may be more common for spaceborne gravitational wave detection,” *Phys. Rev. D* **104**, 063007 (2021), [arXiv:2104.01208 \[astro-ph.HE\]](#).

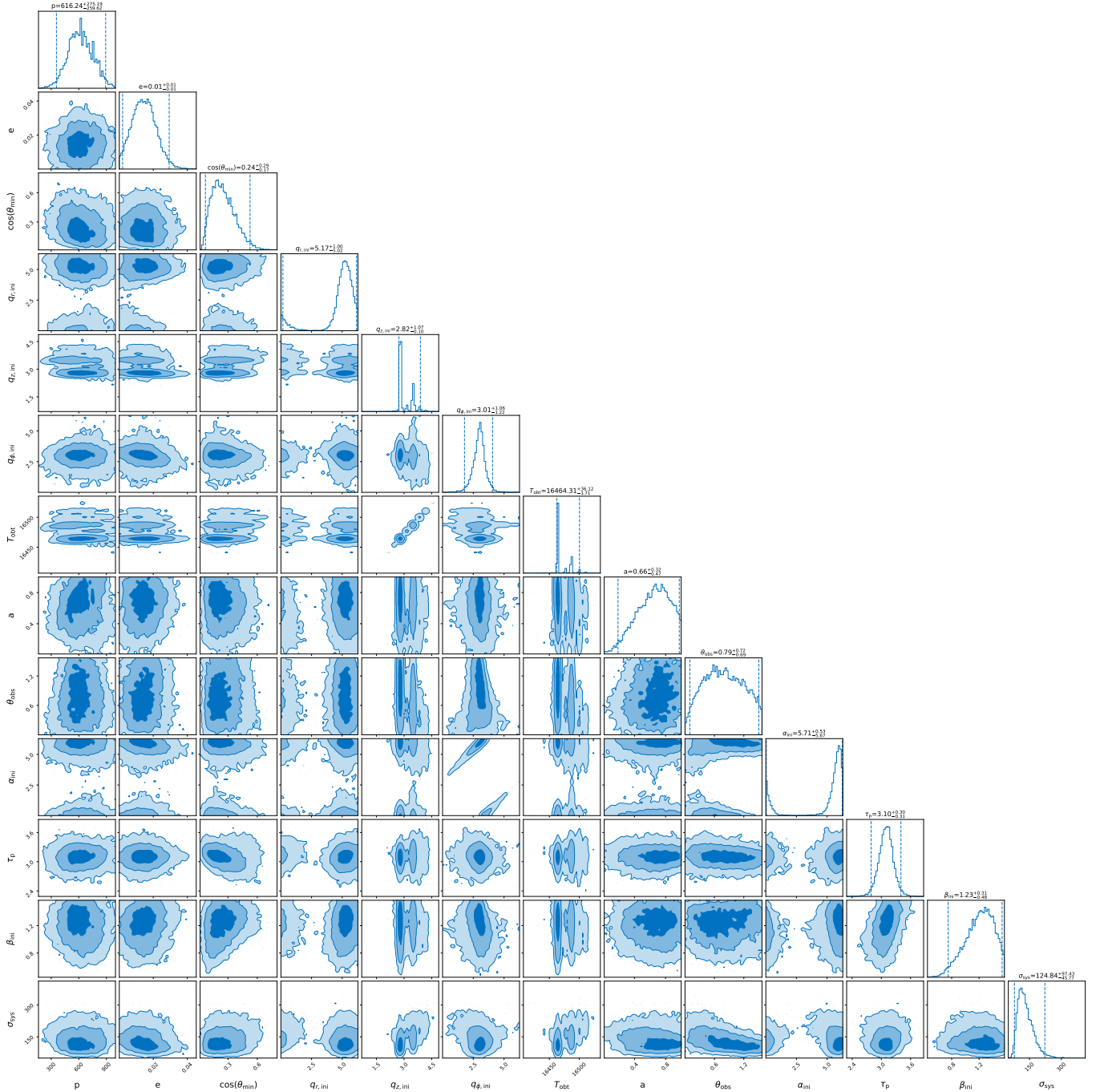


FIG. 8. The posterior corner plot of model parameters for eRO-QPE2 with the hypothesis of an initially misaligned disk ( $\mathcal{H}_1 = \mathcal{H}_{e0} + \mathcal{H}_{df}$ ):  $p[M_\odot]$ ,  $e$ ,  $\cos \theta_{\min}$ ,  $q_{r,\text{ini}}$ ,  $q_{z,\text{ini}}$ ,  $q_{\phi,\text{ini}}$ ,  $T_{\text{obs}}[\text{sec}]$ ,  $a$ ,  $\theta_{\text{obs}}$ ,  $\alpha_{\text{ini}}$ ,  $\tau_p[\text{days}]$ ,  $\beta_{\text{ini}}$ ,  $\sigma_{\text{sys}}[\text{sec}]$ , where each pair of vertical lines denotes the  $2\text{-}\sigma$  confidence level.

- [42] Zhen Pan and Huan Yang, “Supercritical Accretion of Stellar-mass Compact Objects in Active Galactic Nuclei,” *Astrophys. J.* **923**, 173 (2021), [arXiv:2108.00267 \[astro-ph.HE\]](#).
- [43] Zhen Pan, Zhenwei Lyu, and Huan Yang, “Mass-gap extreme mass ratio inspirals,” *Phys. Rev. D* **105**, 083005 (2022), [arXiv:2112.10237 \[astro-ph.HE\]](#).
- [44] Andrea Derdzinski and Lucio Mayer, “In situ extreme mass ratio inspirals via subparsec formation and migration of stars in thin, gravitationally unstable AGN discs,” *MNRAS* **521**, 4522–4543 (2023), [arXiv:2205.10382 \[astro-ph.GA\]](#).
- [45] Yihan Wang, Zhaohuan Zhu, and Douglas N. C. Lin, “Stellar/BH Population in AGN Disks: Direct Binary Formation from Capture Objects in Nuclei Clusters,” *arXiv e-prints*, [arXiv:2308.09129 \(2023\)](#), [arXiv:2308.09129 \[astro-ph.GA\]](#).
- [46] Yihan Wang, Douglas N. C. Lin, Bing Zhang, and Zhaohuan Zhu, “Changing-Look AGN Behaviour Induced by

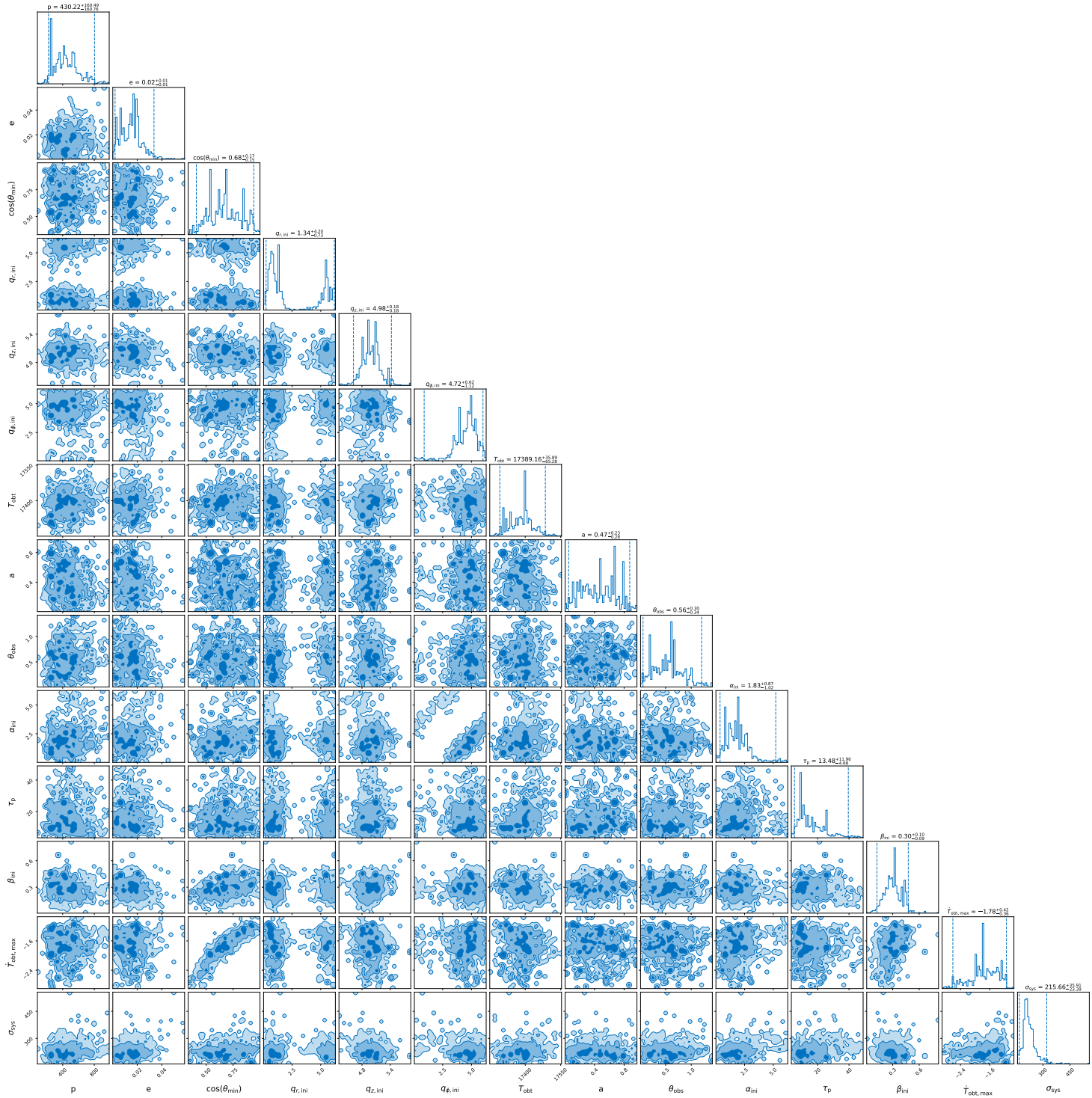


FIG. 9. The posterior corner plot of model parameters for eRO-QPE2 with the hypothesis of a nonuniform orbital decay and a precessing disk ( $\mathcal{H}_2 = \mathcal{H}_{c1} + \mathcal{H}_{ds}$ ):  $p[M_\odot]$ ,  $e$ ,  $\cos \theta_{\min}$ ,  $q_{r,\text{ini}}$ ,  $q_{z,\text{ini}}$ ,  $q_{\phi,\text{ini}}$ ,  $T_{\text{obs}}[\text{sec}]$ ,  $a$ ,  $\theta_{\text{obs}}$ ,  $\alpha_{\text{ini}}$ ,  $\tau_p[\text{days}]$ ,  $\beta_{\text{ini}}$ ,  $\dot{T}_{\text{obs,max}}[\times 10^{-5}]$ ,  $\sigma_{\text{sys}}[\text{sec}]$ , where each pair of vertical lines denotes the  $2\text{-}\sigma$  confidence level.

- [47] Clovis Hopman and Tal Alexander, “The Orbital Statistics of Stellar Inspiral and Relaxation near a Massive Black Hole: Characterizing Gravitational Wave Sources,” *Astrophys. J.* **629**,

- 362–372 (2005), arXiv:astro-ph/0503672 [astro-ph].  
 [48] Miguel Preto and Pau Amaro-Seoane, “On Strong Mass Segregation Around a Massive Black Hole: Implications for Lower-Frequency Gravitational-Wave Astrophysics,” *Astrophys. J. Lett.* **708**, L42–L46 (2010), arXiv:0910.3206 [astro-ph.GA].

- [49] Ben Bar-Or and Tal Alexander, “Steady-state Relativistic Stellar Dynamics Around a Massive Black hole,” *Astrophys. J.* **820**, 129 (2016), [arXiv:1508.01390 \[astro-ph.GA\]](#).
- [50] Stanislav Babak, Jonathan Gair, Alberto Sesana, Enrico Barausse, Carlos F. Sopuerta, Christopher P. L. Berry, Emanuele Berti, Pau Amaro-Seoane, Antoine Petiteau, and Antoine Klein, “Science with the space-based interferometer LISA. V. Extreme mass-ratio inspirals,” *Phys. Rev. D* **95**, 103012 (2017), [arXiv:1703.09722 \[gr-qc\]](#).
- [51] Pau Amaro-Seoane, “Relativistic dynamics and extreme mass ratio inspirals,” *Living Reviews in Relativity* **21**, 4 (2018), [arXiv:1205.5240 \[astro-ph.CO\]](#).
- [52] Luca Broggi, Elisa Bortolas, Matteo Bonetti, Alberto Sesana, and Massimo Dotti, “Extreme mass ratio inspirals and tidal disruption events in nuclear clusters - I. Time-dependent rates,” *MNRAS* **514**, 3270–3284 (2022), [arXiv:2205.06277 \[astro-ph.GA\]](#).
- [53] M. Coleman Miller, Marc Freitag, Douglas P. Hamilton, and Vanessa M. Lauburg, “Binary Encounters with Supermassive Black Holes: Zero-Eccentricity LISA Events,” *Astroph.J.Lett.* **631**, L117–L120 (2005), [arXiv:astro-ph/0507133 \[astro-ph\]](#).
- [54] Yael Raveh and Hagai B. Perets, “Extreme mass-ratio gravitational-wave sources: mass segregation and post binary tidal-disruption captures,” *MNRAS* **501**, 5012–5020 (2021), [arXiv:2011.13952 \[astro-ph.GA\]](#).
- [55] Ryuichi Fujita and Wataru Hikida, “Analytical solutions of bound timelike geodesic orbits in Kerr spacetime,” *Class. Quant. Grav.* **26**, 135002 (2009), [arXiv:0906.1420 \[gr-qc\]](#).
- [56] Maarten van de Meent, “Analytic solutions for parallel transport along generic bound geodesics in Kerr spacetime,” *Class. Quant. Grav.* **37**, 145007 (2020), [arXiv:1906.05090 \[gr-qc\]](#).
- [57] Yasushi Mino, “Perturbative approach to an orbital evolution around a supermassive black hole,” *Phys. Rev. D* **67**, 084027 (2003).
- [58] Brandon Carter, “Global Structure of the Kerr Family of Gravitational Fields,” *Physical Review* **174**, 1559–1571 (1968).
- [59] W. Schmidt, “Celestial mechanics in Kerr spacetime,” *Classical and Quantum Gravity* **19**, 2743–2764 (2002), [arXiv:gr-qc/0202090 \[gr-qc\]](#).
- [60] Irwin I. Shapiro, “Fourth test of general relativity,” *Phys. Rev. Lett.* **13**, 789–791 (1964).
- [61] Maximiliano Isi, Katerina Chatziioannou, and Will M. Farr, “Hierarchical Test of General Relativity with Gravitational Waves,” *Phys. Rev. Lett.* **123**, 121101 (2019), [arXiv:1904.08011 \[gr-qc\]](#).
- [62] Scott Tremaine, Karl Gebhardt, Ralf Bender, Gary Bower, Alan Dressler, S. M. Faber, Alexei V. Filippenko, Richard Green, Carl Grillmair, Luis C. Ho, John Kormendy, Tod R. Lauer, John Magorrian, Jason Pinkney, and Douglas Richstone, “The Slope of the Black Hole Mass versus Velocity Dispersion Correlation,” *Astrophys. J.* **574**, 740–753 (2002), [arXiv:astro-ph/0203468 \[astro-ph\]](#).
- [63] Kayhan Gültekin, Douglas O. Richstone, Karl Gebhardt, Tod R. Lauer, Scott Tremaine, M. C. Aller, Ralf Bender, Alan Dressler, S. M. Faber, Alexei V. Filippenko, Richard Green, Luis C. Ho, John Kormendy, John Magorrian, Jason Pinkney, and Christos Siopis, “The  $M$ - $\sigma$  and  $M$ - $L$  Relations in Galactic Bulges, and Determinations of Their Intrinsic Scatter,” *Astrophys. J.* **698**, 198–221 (2009), [arXiv:0903.4897 \[astro-ph.GA\]](#).
- [64] Michael J. Williams, “nessai: Nested sampling with artificial intelligence,” (2021).
- [65] Gregory Ashton, Moritz Hübner, Paul D. Lasky, Colm Talbot, Kendall Ackley, Sylvia Biscoveanu, Qi Chu, Atul Divakarla, Paul J. Easter, Boris Goncharov, Francisco Hernandez Vivanco, Jan Harms, Marcus E. Lower, Grant D. Meadors, Denyz Melchor, Ethan Payne, Matthew D. Pitkin, Jade Powell, Nikhil Sarin, Rory J. E. Smith, and Eric Thrane, “BILBY: A User-friendly Bayesian Inference Library for Gravitational-wave Astronomy,” *Astroph.J.S.* **241**, 27 (2019), [arXiv:1811.02042 \[astro-ph.IM\]](#).
- [66] J. Buchner, A. Georgakakis, K. Nandra, L. Hsu, C. Rangel, M. Brightman, A. Merloni, M. Salvato, J. Donley, and D. Kocevski, “X-ray spectral modelling of the AGN obscuring region in the CDFS: Bayesian model selection and catalogue,” *Astronomy&Astrophysics* **564**, A125 (2014), [arXiv:1402.0004 \[astro-ph.HE\]](#).
- [67] N. I. Shakura and R. A. Sunyaev, “Black holes in binary systems. Observational appearance.” *Astronomy&Astrophysics* **24**, 337–355 (1973).
- [68] Bence Kocsis, Nicolás Yunes, and Abraham Loeb, “Observable signatures of extreme mass-ratio inspiral black hole binaries embedded in thin accretion disks,” *Phys. Rev. D* **84**, 024032 (2011).
- [69] M Nicholl, T Wevers, S R Oates, K D Alexander, G Leloudas, F Onori, A Jerkstrand, S Gomez, S Campana, I Arcavi, P Charalampopoulos, M Gromadzki, N Ihanec, P G Jonker, A Lawrence, I Mandel, S Schulze, P Short, J Burke, C McCully, D Hiramatsu, D A Howell, C Pellegrino, H Abbot, J P Anderson, E Berger, P K Blanchard, G Cannizzaro, T-W Chen, M Dennefeld, L Galbany, S González-Gaitán, G Hosseinzadeh, C Inerra, I Irani, P Kuin, T Müller-Bravo, J Pineda, N P Ross, R Roy, S J Smartt, K W Smith, B Tucker, Ł Wyrzykowski, and D R Young, “An outflow powers the optical rise of the nearby, fast-evolving tidal disruption event at2019qiz,” *Monthly Notices of the Royal Astronomical Society* **499**, 482–504 (2020), <https://academic.oup.com/mnras/article-pdf/499/1/482/33857159/staa2824.pdf>.